arXiv:2609.01393v1 [cond-mat.soft] 1 Sep 2026

Cell size and confinement drive asymmetric cell division through a cortical instability

Da Gao[1,§], Guoye Guan[2,§,†,*], Chao Tang[2,3,‡], Rui Ma[1,4,*]

1 Department of Physics, College of Physical Science and Technology, Xiamen University, Xiamen 361005, People's Republic of China
2 Center for Quantitative Biology, Peking University, Beijing 100871, People's Republic of China
3 Peking-Tsinghua Center for Life Sciences, Academy for Advanced Interdisciplinary Studies, Peking University, Beijing 100871, People's Republic of China
4 Fujian Provincial Key Laboratory for Soft Functional Materials Research, Research Institute for Biomimetics and Soft Matter, Xiamen 361005, People's Republic of China

§These authors contributed equally to this work.
†Current Address: Department of Systems Biology, Harvard Medical School, Boston 02115, United States of America; Department of Data Science, Dana-Farber Cancer Institute, Boston 02215, United States of America
‡Current Address: Center for Interdisciplinary Studies, Westlake University, Hangzhou 310030, People's Republic of China
*** Corresponding authors: ruima@xmu.edu.cn, guanguoye@gmail.com**

Asymmetric cell division — in which a mother cell divides into two daughter cells of unequal size — is a fundamental problem in biology. It is believed that the asymmetry originates from the prior polarization of the mother cell. Here we show that division asymmetry can occur spontaneously even in unpolarized mother cells. Specifically, curvature-dependent active stresses in the cell cortex can lead to this symmetry breaking without any molecular polarity cue if the mother cell is confined within a restricted space. Either reducing the cell size or tightening mechanical confinement triggers the same spontaneous symmetry-breaking instability, in which the contractile ring slips off the equator to yield daughters of unequal volume. In the presence of a polarity cue, this instability cooperates with the cue to program the division asymmetry. The model prediction is compared with the imaging data of *C. elegans* embryogenesis, in which successive cell divisions in a confined eggshell lead to smaller and smaller cell sizes. The measured division asymmetry indeed increases as the cells shrink, and is further amplified when the embryo is mechanically compressed, both in agreement with the model prediction.

Cell division is executed by the actomyosin cortex—a thin, contractile gel beneath the plasma membrane—whose equatorial constriction partitions the cytoplasm into two daughters [1–3]. Whether this partition is symmetric or asymmetric in volume determines cell fate, developmental timing, and tissue architecture [4, 5]. In *Caenorhabditis elegans*, the germline lineage divides asymmetrically while the somatic founder cells it produces divide nearly symmetrically, and the degree of germline size asymmetry follows a precise, reproducible pattern across successive divisions [6, 7]. What physically sets this asymmetry, and how it responds to cell size and mechanical environment, remains an open question.

Three-dimensional time-lapse imaging has produced detailed morphological atlases of these cleavages [6, 8, 9], which reveal a stereotyped pattern of division asymmetry that most accounts attribute to the anterior–posterior polarity established by PAR (partitioning defective) proteins [10–12]: polarity biases cortical contractility and thereby shifts the cleavage plane away from the position set by pure geometry [6]. Embryonic blastomeres, however, rarely divide in isolation. Cleavage proceeds inside a rigid eggshell, and each blastomere is further hemmed in by its neighbours as the embryo subdivides, so that every division takes place within a mechanically confined space [13, 14]. The blastomeres themselves also become progressively smaller with each successive round. The contribution of these geometric factors—cell size and external mechanical confinement—to the degree of size asymmetry has received comparatively little attention.

Active surface theory provides a natural framework for describing the dividing cortex [1, 15–17]. Within this theory, surfaces fall into distinct classes according to which mirror symmetries they break, and the class dictates which active stresses are admissible [17]. Most cortex models belong to the simplest class, which preserves all mirror symmetries and permits only an isotropic active tension. Such surfaces polarize spontaneously rather than furrow [18, 19], so

that generating a cleavage furrow within this class requires the contractile ring to be imposed by hand, through a prescribed enrichment of myosin at the equator [15, 19]. The cortex, however, belongs to a different class, in which the up-down mirror symmetry is broken. Such breaking arises naturally, either from the asymmetric environment of the cortex, whose two faces are bounded by the plasma membrane on one side and by the cytoplasm on the other, or from a gradient of myosin activity across the finite cortical thickness [20] (Fig. 1A, inset; see Discussion). Either source admits active stresses that are linear in the curvature tensor [17], and the shape dynamics they generate have remained largely unexplored.

Here we model the cortex as a closed viscous surface enclosed by an ellipsoidal shell, retaining the curvature-dependent active stresses that its broken up-down symmetry admits and allowing the bending rigidity to be modulated by a polarity cue. No contractile ring is imposed by hand. The cleavage furrow instead emerges from the curvature-dependent active stresses acting on an ellipsoidal cortex whose curvature gradients are set by the confinement. Using dynamic simulations together with numerical continuation of the steady-state branches, we map the division outcomes across cell size and degree of confinement, and test the resulting predictions against three-dimensional time-lapse imaging of wild-type *C. elegans* embryos.

Curvature-dependent active surface model

Because the actin filaments and myosin motors of the cortex turn over on timescales of seconds—far shorter than the minutes-long division process—the cortex behaves as a viscous fluid on the timescale of cytokinesis while resisting bending as an elastic film [15]. We therefore model it as a closed, axisymmetric viscous surface enclosed by an ellipsoidal shell that represents the mechanical confinement of the embryonic environment (Fig. 1A). Cortical flows follow from force balance, $\mathrm{div}(\mathbf{T}) = -\mathbf{f}^{\mathrm{ext}}$, with the total stress $\mathbf{T}$ comprising Helfrich bending elasticity, viscous dissipation, and the active stress generated by myosin motors (Methods).

The active stress is the ingredient specific to this work. Because the up-down symmetry of the cortex is broken, the theory admits active stresses that are linear in the curvature tensor [17],

$$t^a_{ij} = \xi_s \Delta\mu \big(C_{ij} - \tfrac{1}{2} C^k_k g_{ij}\big) + \xi_b \Delta\mu\, C^k_k g_{ij}, \tag{1}$$

where $\Delta\mu$ is the chemical energy released per ATP hydrolysis cycle, and $\xi_s\Delta\mu$ and $\xi_b\Delta\mu$ quantify how efficiently the motors couple this output to the deviatoric and isotropic components of the cortical curvature. For an axisymmetric surface, the ξ_s term is proportional to the principal curvature difference $C^\phi_\phi - C^u_u$ and the ξ_b term to the mean curvature $C^k_k = C^\phi_\phi + C^u_u$. A cell confined within an ellipsoidal shell adopts an ellipsoidal resting shape in which $C^\phi_\phi - C^u_u$ is maximal at the equator and C^k_k is larger near the poles. The ξ_s term therefore concentrates anisotropic contractile stress at the equator, while the ξ_b term generates extensile isotropic stress near the poles (Fig. 1B,C). Throughout, cell size is measured by the reduced mother-cell radius $\tilde{R}_0 = R_0/L_h$, with L_h the hydrodynamic length, and confinement by the volume ratio $\epsilon = V_{\mathrm{cell}}/V_{\mathrm{shell}}$ (Methods).

Figure 1C,D presents the two characteristic dynamics of cortical shape evolution predicted by the model. In the symmetric case (Fig. 1C; Supplementary Movie 1), the cortex changes from a smooth ellipsoid through a shallow equatorial groove into two nearly spherical lobes joined by an increasingly narrow neck, the furrow tightening symmetrically about the equator. In the asymmetric case (Fig. 1D; Supplementary Movie 2), mirror symmetry is spontaneously broken and the furrow forms off the equator, migrating toward one pole to yield daughter cells of unequal volume. The mechanical origin of the symmetric furrowing lies in the principal curvatures at the furrow. Mapping the two active stress components $(t^a)^u_u$ and $(t^a)^\phi_\phi$ in the principal-curvature plane (C^u_u, C^ϕ_ϕ) (Fig. 1B) and tracking the furrow curvature through successive stages (dots) shows that as the furrow deepens C^u_u becomes increasingly negative and C^ϕ_ϕ increasingly positive, making $(t^a)^\phi_\phi$ progressively more contractile and driving the ring to narrow against bending resistance. The resulting active force density $\mathbf{f}^a = \mathrm{div}(\mathbf{T}^a)$ (red arrows, Fig. 1C,D) concentrates ever more strongly at the constriction as it narrows, enabling an extremely deep cleavage furrow. This positive curvature–stress feedback sustains both trajectories, whose normal force balance, decomposed into its active, viscous and elastic contributions, is detailed in Supplementary Fig. S2.

These two outcomes—symmetric and asymmetric division—represent qualitatively distinct solutions of the same active-surface equations. We next explore systematically how the two geometric parameters, $\tilde{R}_0$ and ϵ, select between them (Fig. 2), showing that both can trigger the underlying symmetry-breaking instability.

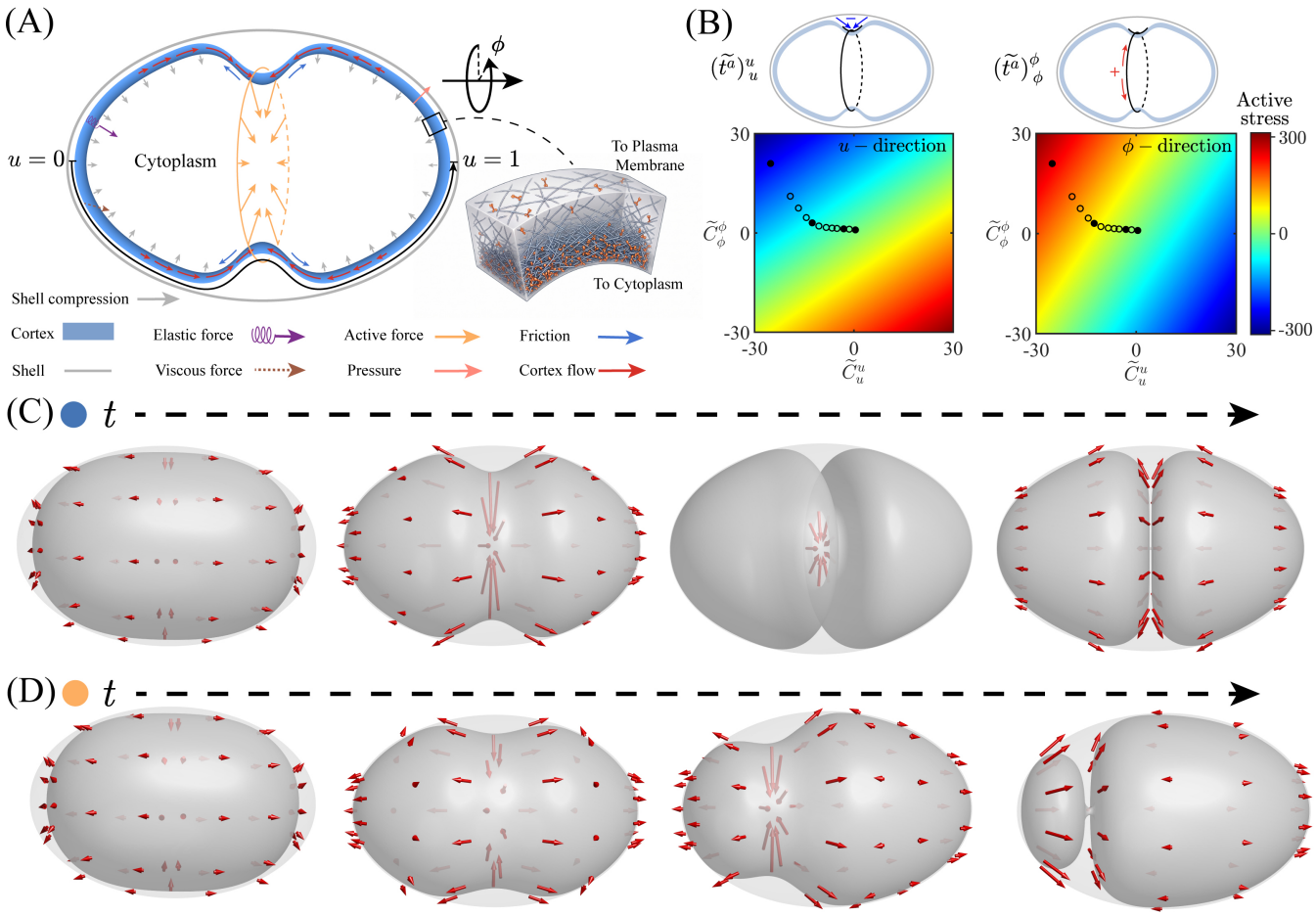


Figure 1. Curvature-guided active surface model for cell division under spatial confinement. **A**, Axisymmetric active-surface model: the cortex is a closed viscoelastic surface $\mathbf{X}(u, \phi, t)$ inside an ellipsoidal confining shell (semi-transparent gray). The model incorporates the curvature-dependent active stress, the elastic and viscous stresses of the cortex, the frictional force, and the intracellular pressure; the cortical shape and flow $\mathbf{v}$ are determined by the force-balance equation [Eq. (3)]. The color gradient across the cortex thickness marks its broken up-down symmetry (cytoplasm-facing, dark; membrane-facing, light); inset: cross-section of the cortex showing the actin network (blue) and myosin motors (orange), whose density increases toward the cytoplasmic face—a possible microscopic origin of the curvature-dependent active stress (see Discussion). **B**, Active stress components $(t^a)^u_u$, $(t^a)^\phi_\phi$ in the principal-curvature plane (C^u_u, C^ϕ_ϕ). Dots trace the furrow curvature during the symmetric division of C, the four black solid dots marking the four snapshots shown there. **C,D**, Snapshots of a symmetric (C) and asymmetric (D) division. Red arrows, active force density $\mathbf{f}^a = \mathrm{div}(\mathbf{T}^a)$. In the third snapshot of C, arrows are visible only near the equator because $\mathbf{f}^a$ has become too small elsewhere to display, reflecting the progressive concentration of the active force at the constriction. Symmetry breaking in D shifts the furrow off-equator, yielding daughters of unequal volume.

Size and confinement control division symmetry

To clarify how cell size governs the symmetry of division, we perform dynamic simulations for various cell sizes $\tilde{R}_0$ at fixed confinement $\epsilon = 0.87$, so that the shell volume is reduced in proportion to the cell as $\tilde{R}_0$ decreases. Three distinct outcomes emerge (Fig. 2A). For large cells, a constriction furrow nucleates at the equatorial plane and narrows symmetrically, yielding daughter cells of equal volume, quantified by the division asymmetry index $\chi = (V_b - V_s)/(V_b + V_s) \approx 0$, where V_b and V_s are the volumes of the bigger and smaller daughter cells. At intermediate $\tilde{R}_0$, the furrow likewise initiates at the equator but, as it narrows, its position—the locus where the meridional curvature C_u^u is most negative—spontaneously slips toward one pole, yielding daughters of unequal volume with χ increasing continuously as $\tilde{R}_0$ decreases. For very small cells, the cortex forms only a weakly invaginated furrow and fails to constrict further, arresting cytokinesis (Supplementary Movie 3). The phase diagram of Fig. 2B shows that decreasing $\tilde{R}_0$ progressively raises the symmetry-breaking threshold $\tilde{\xi}_s^*$ and expands the failed-division region, so that smaller cells require stronger motor activity to break equatorial symmetry but, once the threshold is exceeded, produce greater division asymmetry.

To resolve the underlying mechanism, we use numerical continuation to compute the steady-state solution branches as a function of $\tilde{\xi}_s$ at two representative radii, $\tilde{R}_0 = 1.64$ and 2.00 (Fig. 2C,E; Methods). Two classes of solutions are distinguished by their symmetry: a red branch of geometries that preserve mirror symmetry about the equatorial plane, which at $\tilde{\xi}_s = 0$ adopts the ellipsoidal shape imposed by the confining shell, and an orange branch of geometries whose furrow is displaced off the equator. At a critical activity $\tilde{\xi}_s^*$ the symmetric branch loses stability and the asymmetric branch bifurcates from it. At still higher activity the symmetric branch reaches a turning point and folds back, beyond which no symmetric steady state exists. These two thresholds partition the $\tilde{\xi}_s$ axis into exactly the three regimes found dynamically in Fig. 2A. Below the bifurcation the symmetric branch is stable and the cortex settles onto it, giving failed division. Between the bifurcation and turning points the symmetric branch is unstable, so mirror symmetry breaks and division is asymmetric. Beyond the turning point no symmetric steady state remains and the cortex constricts symmetrically until the furrow radius becomes extremely small. At the activity used in Fig. 2A, $\tilde{R}_0 = 1.64$ lies below the bifurcation and $\tilde{R}_0 = 2.00$ within the asymmetric window, reproducing the failed and asymmetric outcomes respectively.

Near threshold, the displacement of the ring from the equator, $\Delta u = u_{\text{furrow}} - 0.5$, follows the square-root scaling $|\Delta u| \propto |\tilde{\xi}_s - \tilde{\xi}_s^*|^{1/2}$ characteristic of a pitchfork bifurcation (Fig. 2D,F; Supplementary Fig. S3). Its character changes with cell size: the transition is supercritical at $\tilde{R}_0 = 2.00$ and subcritical at $\tilde{R}_0 = 1.64$.

The same analysis along the confinement axis yields the same three-regime structure. Computing χ against ϵ at fixed $\tilde{R}_0 = 2.22$ gives symmetric division at weak confinement, a continuous rise in χ above a critical ϵ, and division failure beyond $\epsilon_c \approx 0.895$ (Fig. 2G), and the phase diagram of Fig. 2H shows that tightening confinement raises $\tilde{\xi}_s^*$ and expands the failed-division region exactly as decreasing $\tilde{R}_0$ does. The branch structure and its correspondence with the dynamics are likewise unchanged (Fig. 2I,K). Two features are specific to this axis. First, the bifurcation character shifts in the opposite sense, being supercritical at $\epsilon = 0.88$ and subcritical at $\epsilon = 0.64$ (Fig. 2J,L), whereas along the size axis it becomes subcritical as the cell shrinks. Second, at weak confinement the symmetric branch acquires an S-shaped structure, so that an ellipsoidal state without ingression and an already-furrowed state coexist as stable solutions over a range of $\tilde{\xi}_s$ (Fig. 2I). At an even weaker confinement, $\epsilon = 0.56$, the two folds of this S swap their order along $\tilde{\xi}_s$, so that increasing activity carries the cortex from failed division directly to symmetric constriction, eliminating the asymmetric-division window altogether (Supplementary Fig. S4).

Cell size and confinement therefore act on one and the same active-surface instability, providing a unified mechanical basis for how geometric cues set the degree of division asymmetry.

Polarity regulation biases the division plane

Embryonic cytokinesis is typically also guided by an intrinsic polarity cue. To incorporate one while preserving the mechanical responses identified above, we modulate the cortical bending rigidity locally,

$$\kappa(u) = \kappa_0 \left[1 + \Delta_\kappa \exp\left(-\frac{(u - u_0)^2}{\omega^2}\right)\right], \tag{2}$$

a Gaussian pulse centered at u_0 with width ω and amplitude Δ_κ (Fig. 3A). Modulating κ is mechanistically motivated: the contractile ring is enriched in actin filaments and crosslinking proteins relative to the surrounding cortex [1, 21], so the bending rigidity is locally elevated at the ring, and both crosslinker density and actin network architecture are downstream targets of PAR polarity proteins in *C. elegans* [22–24]. How faithfully the cue encodes a division plane depends on its width and amplitude. For narrow profiles the daughter-cell asymmetry χ varies near-linearly with the

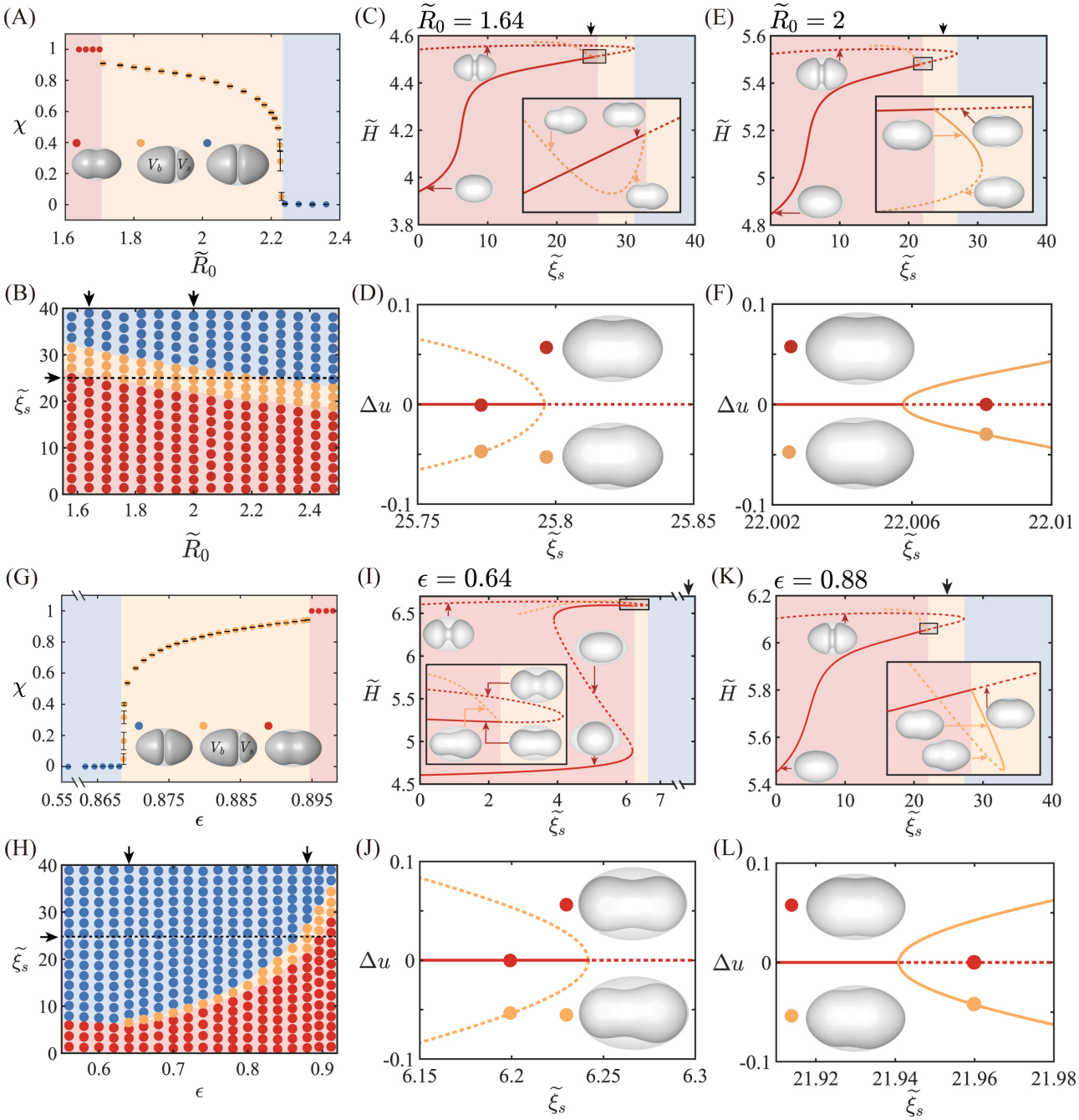


Figure 2. Cell size and confinement both trigger a symmetry-breaking instability. Panels **A**–**F** vary cell size at fixed confinement ($\epsilon = 0.87$), panels **G**–**L** vary confinement at fixed size ($\tilde{R}_0 = 2.22$). **A,G**, Division asymmetry χ versus cell radius $\tilde{R}_0$ (**A**) and shell confinement ϵ (**G**), revealing three regimes: symmetric ($\chi \approx 0$, blue), asymmetric (orange), and failed division (red). Failed divisions are assigned $\chi = 1$, as no partition is completed. Error bars denote the standard deviation over ten simulations, each with a different random perturbation of the active stress applied at the first time step (Supplementary Information). **B,H**, Phase diagrams in the $(\tilde{R}_0, \tilde{\xi}_s)$ and $(\epsilon, \tilde{\xi}_s)$ planes. In each, the two arrows above mark the parameter values examined in the panels to the right, and the arrow on the left, with the dashed horizontal line, marks the activity $\tilde{\xi}_s$ used in the dynamic simulations of **A** and **G**. **C,E,I,K**, Steady-state bifurcation landscapes ($\tilde{H}$ vs. $\tilde{\xi}_s$) at $\tilde{R}_0 = 1.64$ and 2.00 (**C,E**) and $\epsilon = 0.64$ and 0.88 (**I,K**). Solid and dashed branches denote stable and unstable solutions, insets show representative cortex shapes, and the arrow above each panel marks the same activity $\tilde{\xi}_s$ as in **A,G**. In **I** the symmetric branch is S-shaped, so that an ellipsoidal state without ingression and a furrowed state coexist as stable solutions over a range of $\tilde{\xi}_s$. **D,F,J,L**, Contractile-ring displacement $|\Delta u|$ near the symmetry-breaking threshold $\tilde{\xi}_s^*$ ($\tilde{\xi}_s^* = 25.796$ and 22.006 in **D,F**, and 6.24 and 21.94 in **J,L**). In both sweeps, decreasing cell size or tightening confinement raises $\tilde{\xi}_s^*$, expands the failed-division region, and produces stronger asymmetry above threshold. The bifurcation character, however, shifts in opposite senses along the two control parameters: from supercritical to subcritical as the cell size decreases (**D,F**), but from subcritical to supercritical as the confinement tightens (**J,L**).

cue offset Δu, so that small displacements translate into proportional changes of χ, whereas broader profiles flatten the relation and decouple cue position from division outcome (Fig. 3B). The amplitude controls the sensitivity of the response (Fig. 3C): below a threshold the cortex fails to track the cue, and at large Δ_κ the response saturates. Narrow profiles of intermediate amplitude therefore define the operating window for high-fidelity polarity encoding.

Coupling the polarity profile to the geometric control parameters produces two distinct trends. Along the cell-size axis, χ approaches a constant set by the cue offset u_0 alone for large cells, and rises sharply once the cell-size induced instability of Fig. 2A takes over at small $\tilde{R}_0$ and progressively amplifies the polarity-induced asymmetry (Fig. 3D). The arrows mark the radii of the four successive germline blastomeres, set recursively from the P0 zygote, whose size is the single calibrated input: each germline division produces two daughters and the smaller one becomes the next germline cell, so that the arrows track the shrinking lineage along the curve. We show below that this predicted escalation is qualitatively consistent with the measured P0–P3 trend (Fig. 5D). Along the confinement axis, χ likewise approaches a constant set by u_0 in the weak-confinement limit and is then amplified monotonically as confinement tightens (Fig. 3E), so confinement and polarity act cooperatively to enhance unequal partitioning.

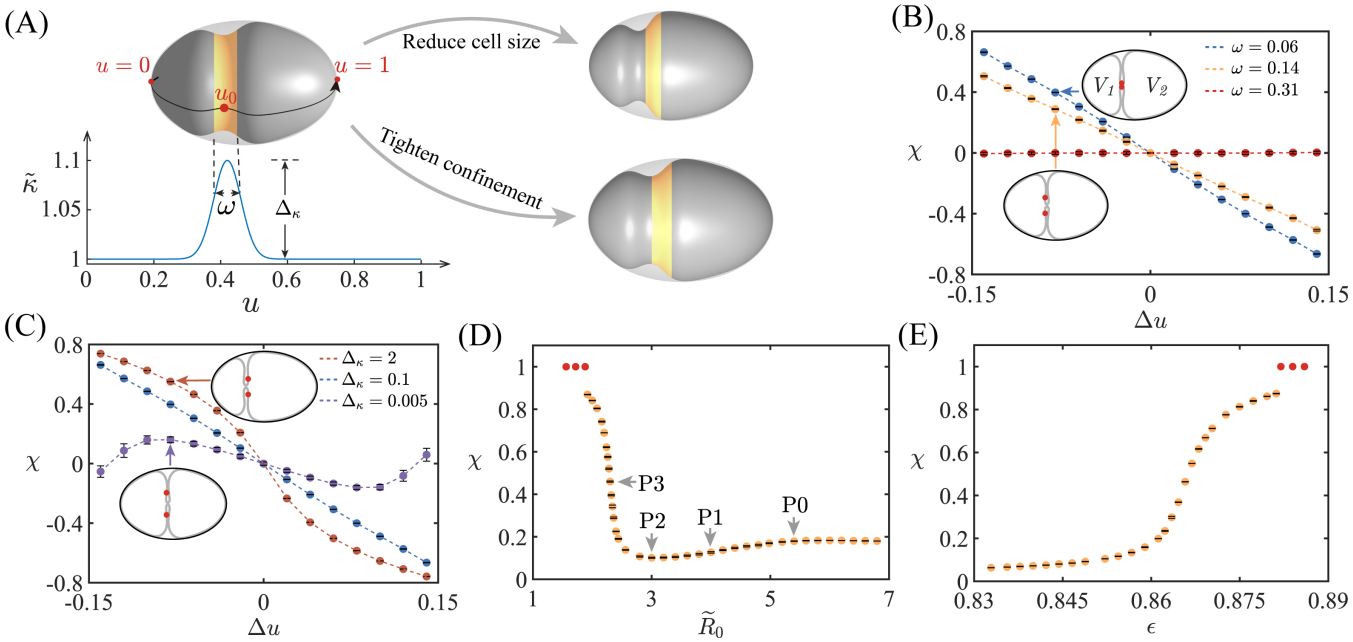


Figure 3. Localized polarity regulation specifies the position and magnitude of asymmetric division. A, Left: bending-rigidity profile $\tilde{\kappa}(u) = 1 + \Delta_\kappa \exp[-(u-u_0)^2/\omega^2]$, a Gaussian pulse of width ω and amplitude Δ_κ centered off the equator at u_0, which biases the contractile ring toward u_0. Right: cortex shapes for reduced cell size (upper) and reduced shell size (lower). **B,C**, Division asymmetry χ versus the polarity offset $\Delta u = u_0 - 0.5$ at $\tilde{R}_0 = 5.4$, for profile widths $\omega = 0.06, 0.14, 0.31$ (**B**) and amplitudes $\Delta_\kappa = 0.005, 0.1, 2$ (**C**). A narrow profile gives a near-linear response, broader ones flatten it, and the intermediate amplitude ($\Delta_\kappa = 0.1$) defines the high-fidelity operating window. Insets in **B** and **C**: cortex shapes at the marked points, both red dots marking the prescribed cue position u_0. In **B** the furrow coincides with u_0 for $\omega = 0.06$ (upper) but is displaced from it for $\omega = 0.14$ (lower), so that the cue no longer faithfully sets the division plane. In **C** a strong cue ($\Delta_\kappa = 2$, upper) drives the furrow beyond u_0, producing an asymmetry stronger than u_0 alone would set, whereas a weak cue ($\Delta_\kappa = 0.005$, lower) leaves the furrow short of u_0, producing a weaker one. **D,E**, χ versus cell radius $\tilde{R}_0$ at fixed $\epsilon = 0.87$ (**D**, arrows mark the P0–P3 radii), and versus shell confinement ϵ at fixed $\tilde{R}_0 = 2.22$ (**E**). Both use the same polarity profile, $u_0 = 0.465$, $\omega = 0.06$ and $\Delta_\kappa = 0.1$. χ is nearly constant at large $\tilde{R}_0$ and rises sharply at small $\tilde{R}_0$, and increases monotonically with ϵ. Red dots: division failure. Error bars in **B**–**E** denote the standard deviation over ten simulations, each with a different random perturbation of the active stress applied at the first time step (Supplementary Information).

Model captures embryonic morphology and lineage

To validate the model against experiment, we compare simulated cortex contours with cell boundaries extracted from time-lapse imaging of the first (P0 cell) cleavage in *C. elegans* [25, 26]. At six successive time points spanning the full constriction sequence—from the initial ellipsoidal configuration through progressive furrow deepening to near-complete division—the simulated contour (red) closely follows the experimental boundary (black), achieving a similarity index exceeding 90% (Fig. 4A; Supplementary Movie 4; defined in Methods). This quantitative agreement

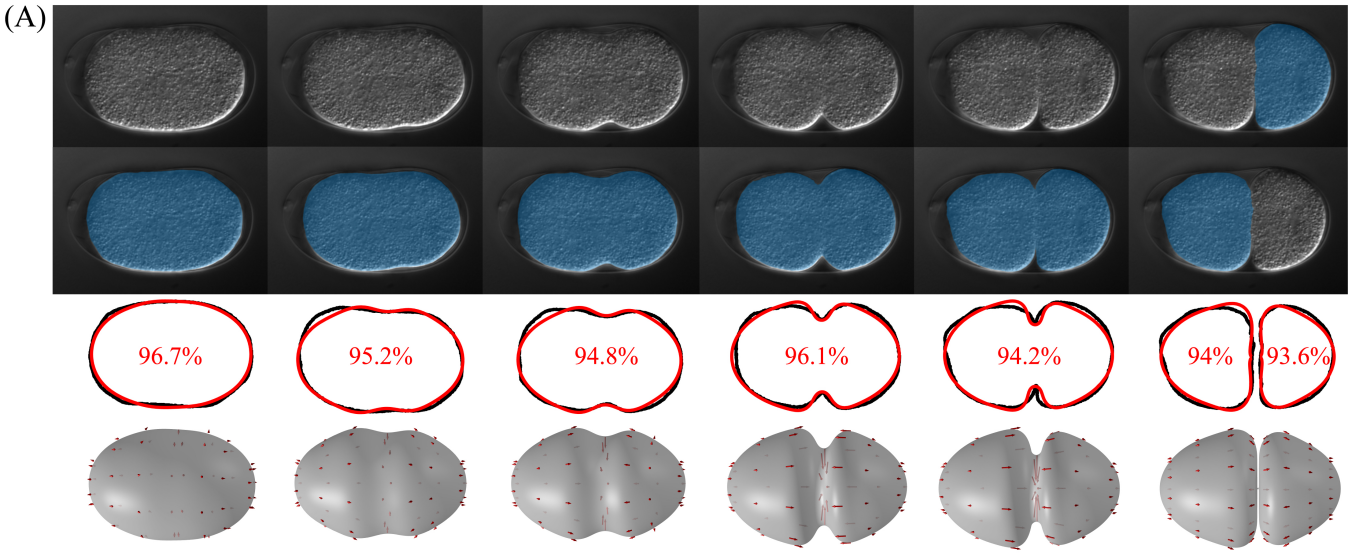
confirms that the model parameter set, with the shell confinement fixed at $\epsilon = 0.87$, faithfully captures the cortex geometry throughout the division process.

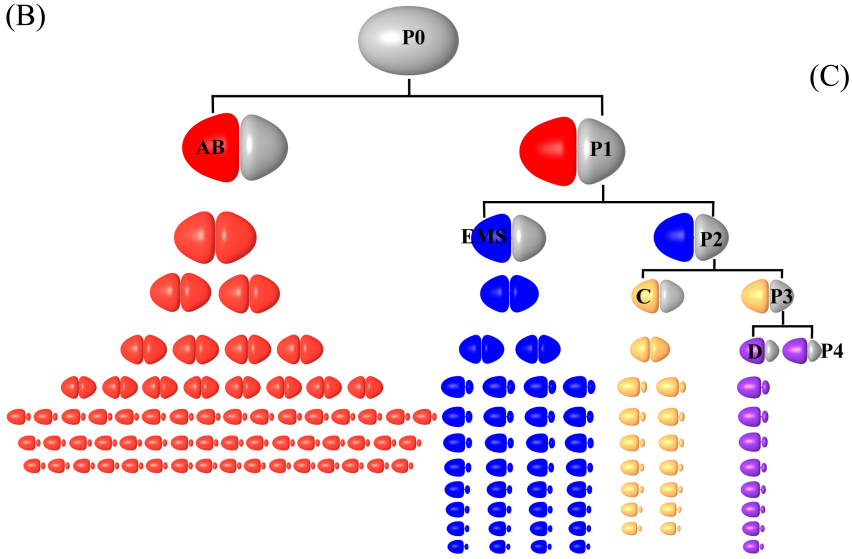
We next ask whether the same framework can reproduce the complete early embryonic division pattern. Guided by the known *C. elegans* lineage [27], we let the somatic blastomeres (AB, EMS, C, and D) divide by self-organized mechanics alone and add the localized κ-modulation of Fig. 3 to the successive germline divisions (P0–P3). All cells share a single parameter set (Supplementary Table S3) at the same fixed shell confinement $\epsilon = 0.87$, and only the cell size decreases during cleavage. The one calibrated input is the P0 zygote radius $\tilde{R}_0 = 5.4$, chosen to match the measured germline asymmetries of Fig. 5D. From this starting point the model generates a lineage tree that captures the experimentally observed division pattern (Fig. 4B). The AB lineage divides symmetrically while its cells remain large, producing an expanding array of equal-sized daughters. As the cells shrink, the size-induced instability eventually drives these somatic divisions asymmetric as well, a prediction we test against the AB lineage below (Fig. 5C). The germline P blastomeres, by contrast, divide with progressively stronger asymmetry throughout, a prediction we compare directly against the measured germline series below (Fig. 5D,E). The tree is built in a volume-driven manner. The two daughter volumes computed at each division become the inputs to the next round. The size at which divisions stop follows from the bifurcation analysis: it is the critical radius $\tilde{R}_{0,c}$ at which the fixed-activity trajectory crosses the pitchfork boundary $\tilde{\xi}_s = \tilde{\xi}_s^*(\tilde{R}_{0,c}, \epsilon)$ into the failed-division regime (Fig. 2A,B, and Fig. 3D for the polarity-regulated germline). Below $\tilde{R}_{0,c}$ the mirror-symmetric branch is stable and the cortex relaxes to a weakly invaginated state, so the branch terminates. A generation whose cell number fails to double therefore marks an asymmetric division whose smaller daughter has dropped below $\tilde{R}_{0,c}$, and the lineage ends once all remaining cells lie in the failed-division regime. The model reproduces the finite number of divisions in every founder lineage, matching the measured count to within a single round for the EMS and P lineages, although lineage-specific deviations elsewhere show that size and confinement alone do not fix the exact number of rounds (Fig. 4C). Taken together, these results show that the interplay between self-organized active-surface instability and localized polarity regulation captures the main features of the early division pattern, while additional control beyond geometry contributes to setting how many times each lineage divides.

Embryonic data support geometric control

To assess whether the mechanical trends identified in the model are operative in living embryos, we analyse two public four-dimensional morphological datasets of *C. elegans* embryogenesis: *CMap*, comprising 8 mechanically uncompressed embryos, and *CShaper*, comprising 17 mechanically compressed embryos [29, 30]. Membrane and nuclear labels resolve every division and identify it by lineage across embryos (Fig. 5A), so that each embryo contributes one value of χ per division event (Supplementary Information).

Pooling all division events from the *CMap* dataset and binning by mother-cell volume reveals that χ increases systematically as cell size decreases (Fig. 5B), in direct agreement with the model prediction of Fig. 2A. Representative examples from the AB somatic lineage (ABa $\rightarrow$ ABal $\rightarrow$ ABalap $\rightarrow$ ABalaa) show that division asymmetry escalates continuously as cells shrink through successive rounds of cleavage, confirming the prediction that even somatic divisions become asymmetric once the cells are sufficiently small (Fig. 5C). The same holds for the four successive P-lineage divisions, where χ increases with decreasing mean cell volume as the geometric instability progressively dominates the polarity-specified positioning: the asymmetry is statistically indistinguishable between P0 and P1, but rises significantly at P2 and again at P3 (Fig. 5D,E). The P0 size in the model was calibrated to reproduce this measured trend, so that the germline asymmetries computed along the model curve (arrows in Fig. 3D) tie the mechanical prediction directly to experiment. Both model and data show χ staying low across the early germline divisions and rising steeply for the late ones, although the model places this rise at P3, whereas the measured asymmetry is already pronounced at P2.

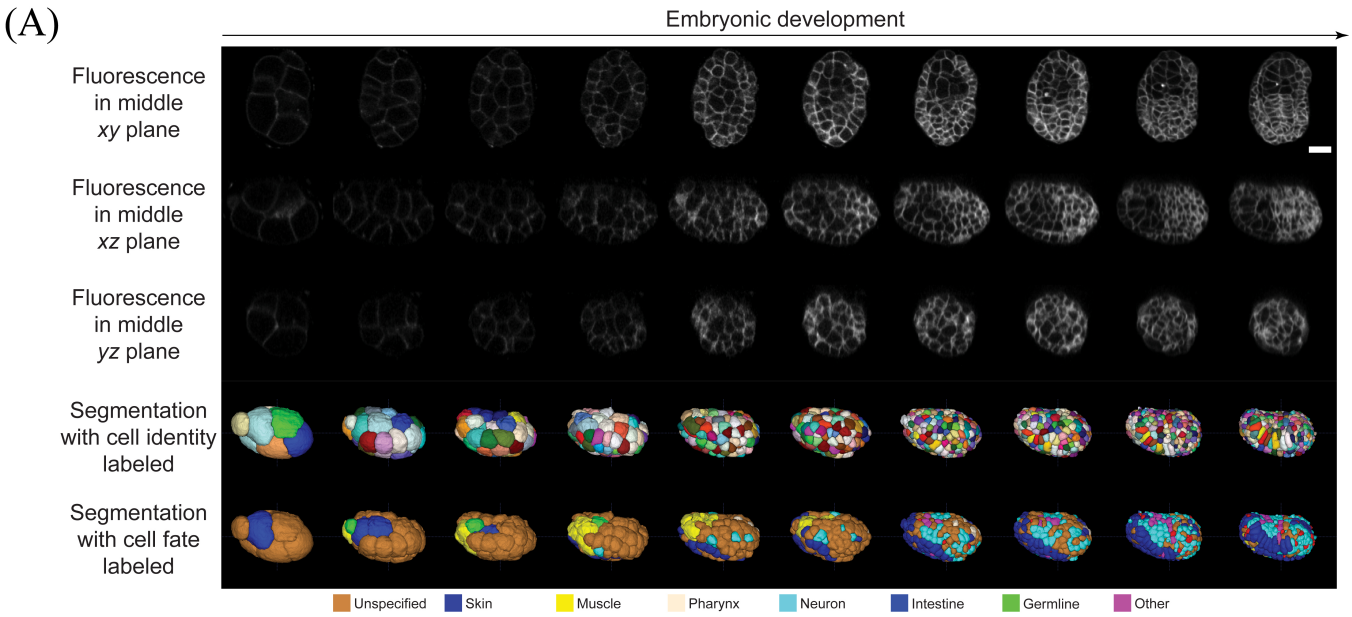


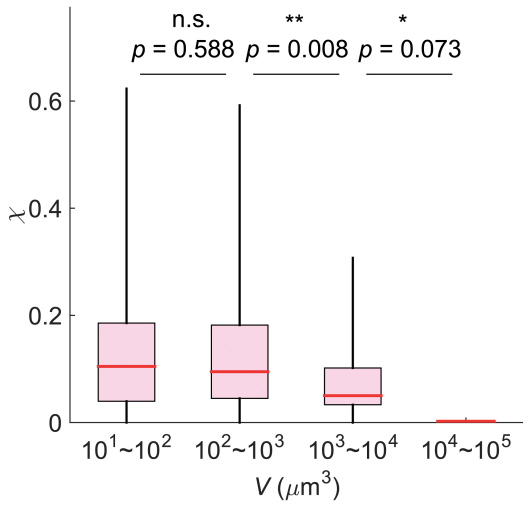


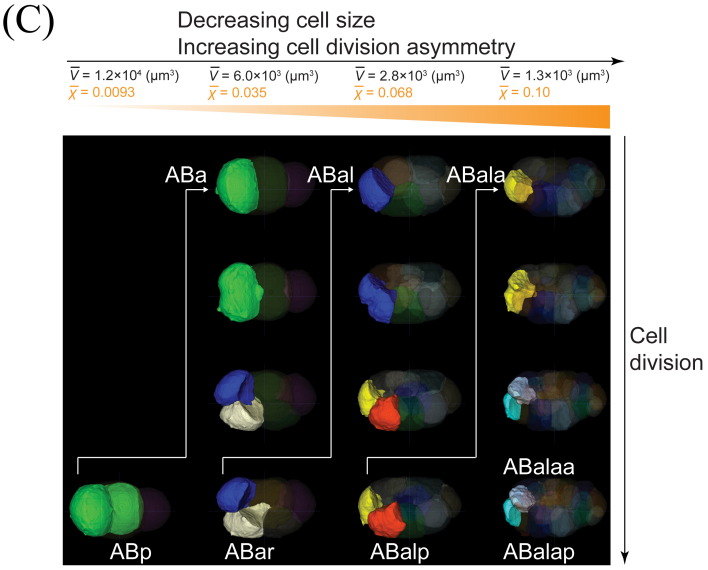
(C) Number of division rounds per lineage

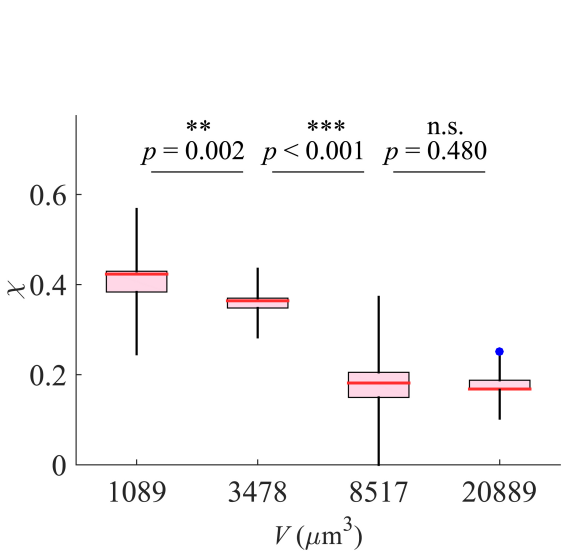
Lineage	Theory	Experiment
AB	7	11
EMS	10	9
D	8	5
P	4	5
C	8	6

Figure 4. Active-surface model reproduces embryonic division morphology and captures the early lineage. A, Simulated and experimental cortex shapes at six time points (columns) of the first (P0 cell) cleavage. Rows, top to bottom: brightfield images; the same images with the automatic segmentation [25, 26] overlaid in blue; axial cross-section contours (simulated in red, segmented experimental boundary in black) annotated with the similarity index (Supplementary Information), which exceeds 90% throughout; and the simulated three-dimensional cortex surface with red arrows showing the active force density. At the final time point the two daughters are shown separately in each row. **B**, Lineage-level simulation of early *C. elegans* divisions from the P0 zygote. Somatic blastomeres (AB, red; EMS, blue; C, orange; D, purple) divide without polarity regulation, and germline blastomeres (P0–P3, gray) divide with the localized κ-modulation of Fig. 3. With a single shared parameter set (shell confinement $\epsilon = 0.87$) and continuously decreasing cell size, the model captures the AB-lineage divisions, symmetric for the first four rounds and asymmetric from the fifth as the cells shrink, together with the progressively asymmetric germline divisions. The two daughter volumes computed at each division are carried forward to the next round. A daughter smaller than the critical radius $\tilde{R}_{0,c}$ set by the pitchfork boundary of Fig. 2 can no longer divide, and the tree terminates once all remaining cells lie in the failed-division regime. **C**, Number of division rounds completed by each founder lineage, predicted by the model and measured *in vivo* [28, 29].


(A)
Embryonic development
Fluorescence in middle xy plane
Fluorescence in middle xz plane
Fluorescence in middle yz plane
Segmentation with cell identity labeled
Segmentation with cell fate labeled
Unspecified
Skin
Muscle
Pharynx
Neuron
Intestine
Germline
Other


(B)
n.s.
p = 0.588
**
p = 0.008
*
p = 0.073
χ
0.6
0.4
0.2
0
10^1~10^2
10^2~10^3
10^3~10^4
10^4~10^5
V (μm^3)


(C)
Decreasing cell size
Increasing cell division asymmetry
V̄ = 1.2×10^4 (μm^3)
χ̄ = 0.0093
V̄ = 6.0×10^3 (μm^3)
χ̄ = 0.035
V̄ = 2.8×10^3 (μm^3)
χ̄ = 0.068
V̄ = 1.3×10^3 (μm^3)
χ̄ = 0.10
ABa
ABal
ABala
ABalaa
ABp
ABar
ABalp
ABalap
Cell division


(D)
**
p = 0.002
***
p < 0.001
n.s.
p = 0.480
χ
0.6
0.4
0.2
0
1089
3478
8517
20889
V (μm^3)

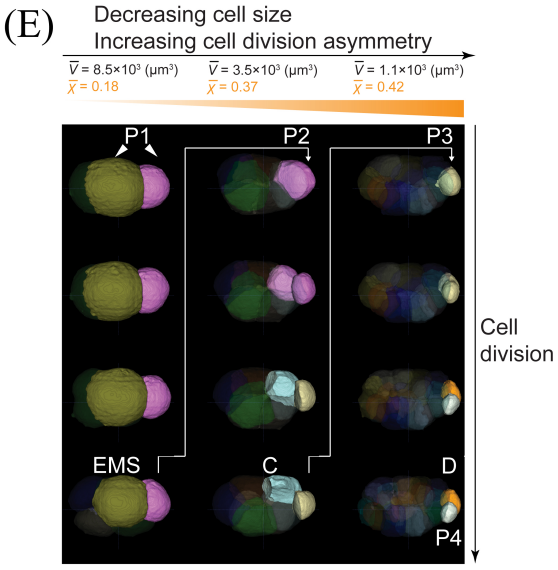

(E)
Decreasing cell size
Increasing cell division asymmetry
V̄ = 8.5×10^3 (μm^3)
χ̄ = 0.18
V̄ = 3.5×10^3 (μm^3)
χ̄ = 0.37
V̄ = 1.1×10^3 (μm^3)
χ̄ = 0.42
P1
P2
P3
EMS
C
D
P4
Cell division

Figure 5. Cell-size-dependent division asymmetry across *C. elegans* embryogenesis. **A**, Time-lapse three-dimensional morphological maps of *C. elegans* embryonic development from the *CMap* dataset [29,30], showing fluorescence images in the middle xy, xz, and yz planes (top three rows) together with cell segmentations colored by cell identity (fourth row) and cell fate (fifth row). **B**, Division asymmetry χ as a function of mother-cell volume V, pooled across all division events and binned into four volume decades (10^1–10^2, 10^2–10^3, 10^3–10^4, 10^4–10^5 μm^3). χ increases as cell size decreases; pairwise comparisons between adjacent bins are annotated (one-sided Wilcoxon rank-sum test; n.s., $p > 0.1$; $^{*}p < 0.1$; $^{**}p < 0.05$). In **B** and **D**, boxes span the first to third quartiles with the median as the central line, whiskers extend to the most extreme values within 3 IQR of the box, where IQR is the interquartile range, and points beyond are plotted as outliers (Supplementary Information). **C**, Representative snapshots illustrating the size-dependent increase in division asymmetry along the AB somatic lineage (ABa, ABal, ABalap, ABalaa), with decreasing mean cell volume (indicated above each panel) and increasing χ (orange bar) from left to right. **D**, Division asymmetry χ as a function of mean cell volume $\bar{V}$ for the four successive P-lineage germline divisions (P0–P3; $\bar{V} = 2.089,\ 0.852,\ 0.348,\ 0.109 \times 10^4\ \mu\text{m}^3$). χ increases with decreasing $\bar{V}$; adjacent-stage comparisons show P0 versus P1, $p = 0.480$ (n.s.); P1 versus P2, $p < 0.001$ (***); and P2 versus P3, $p = 0.002$ (**) (one-sided Wilcoxon rank-sum test). **E**, Representative snapshots of the P-lineage germline blastomeres (P1, P2, P3) and their somatic daughters (EMS, C, D, P4), showing successive rounds of asymmetric cleavage with increasing division asymmetry as cell size decreases.

We next test the prediction that external mechanical confinement amplifies division asymmetry. Comparing all matched division events between the uncompressed (*CMap*, χ_U) and compressed (*CShaper*, χ_C) datasets yields a tight proportional relationship, with a regression slope of 1.151 ($R^2 = 0.917$), indicating that compression amplifies division asymmetry globally by ∼15% relative to the uncompressed baseline (Fig. 6B), consistent with the monotonic increase predicted by the model (Fig. 2G). The compressed embryo is visibly flattened relative to its uncompressed counterpart (Fig. 6A), consistent with the reduced effective shell volume encoded in ϵ, and individual lineages show the same compression-induced increase in χ (Fig. 6C). Together, Figs. 5 and 6 indicate that the cell-size and confinement dependences identified in the model are operative *in vivo*, and that the self-organized and polarity-regulated mechanisms cooperate to set the observed division asymmetry.

Implications and limitations

Asymmetric cell division is a conserved strategy for generating cellular diversity, yet the physical principles that set the degree of asymmetry have remained elusive. Here we established that, beyond the molecular polarity cues usually believed responsible, asymmetric division can also be driven by a mechanical instability of the active cortex. This instability may complement and enhance the polarity-based patterning. Permitted by the broken up-down symmetry of the cortex [17], a curvature-dependent active stress makes symmetric division the default outcome, and either decreasing cell size or tightening confinement destabilizes that symmetry through a pitchfork bifurcation, so that two independent geometric quantities act on a single active-surface instability. Embryonic morphological data support both predicted control parameters.

Although curvature-dependent active stress is permitted by the broken up-down symmetry of the cortex [17], its microscopic origin remains an open question. Active elastic thin-shell theory offers one route [20]: an active stress profile that varies across the finite cortical thickness generates, besides an active tension, an active bending moment, which in a curved shell produces an effective in-plane stress proportional to the local curvature (Methods). Within this picture the coupling coefficients ξ_s and ξ_b in Eq. (1) reflect the gradient of myosin activity across the cortex, so that variations in cortical architecture that alter the transverse distribution of motor activity could directly tune the degree of division asymmetry.

The present model captures cortical mechanics at the cellular scale but does not resolve processes at the subcellular or supracellular level. Cell polarity enters only as a phenomenological modulation of bending rigidity, whereas the underlying anterior–posterior domain is maintained by reaction–diffusion–advection dynamics among PAR proteins on the membrane and in the cytosol [10,12,31,32]. The mechanical influence of neighbouring blastomeres is captured by an idealized ellipsoidal shell rather than by explicit cell–cell contact forces [13,14], the broader context set by global embryonic constraints is not resolved [33,34], and the model assumes axial symmetry, whereas real *C. elegans* blastomeres are non-axisymmetric and subject to three-dimensional spatial constraints [35,36]. A natural path forward is to incorporate the curvature-dependent active stress identified here into a phase-field framework for multicellular morphogenesis [37,38], in which division timing, axis, and volume ratio could emerge self-consistently from the interplay of active cortical stress, cell–cell interactions, and geometric confinement.

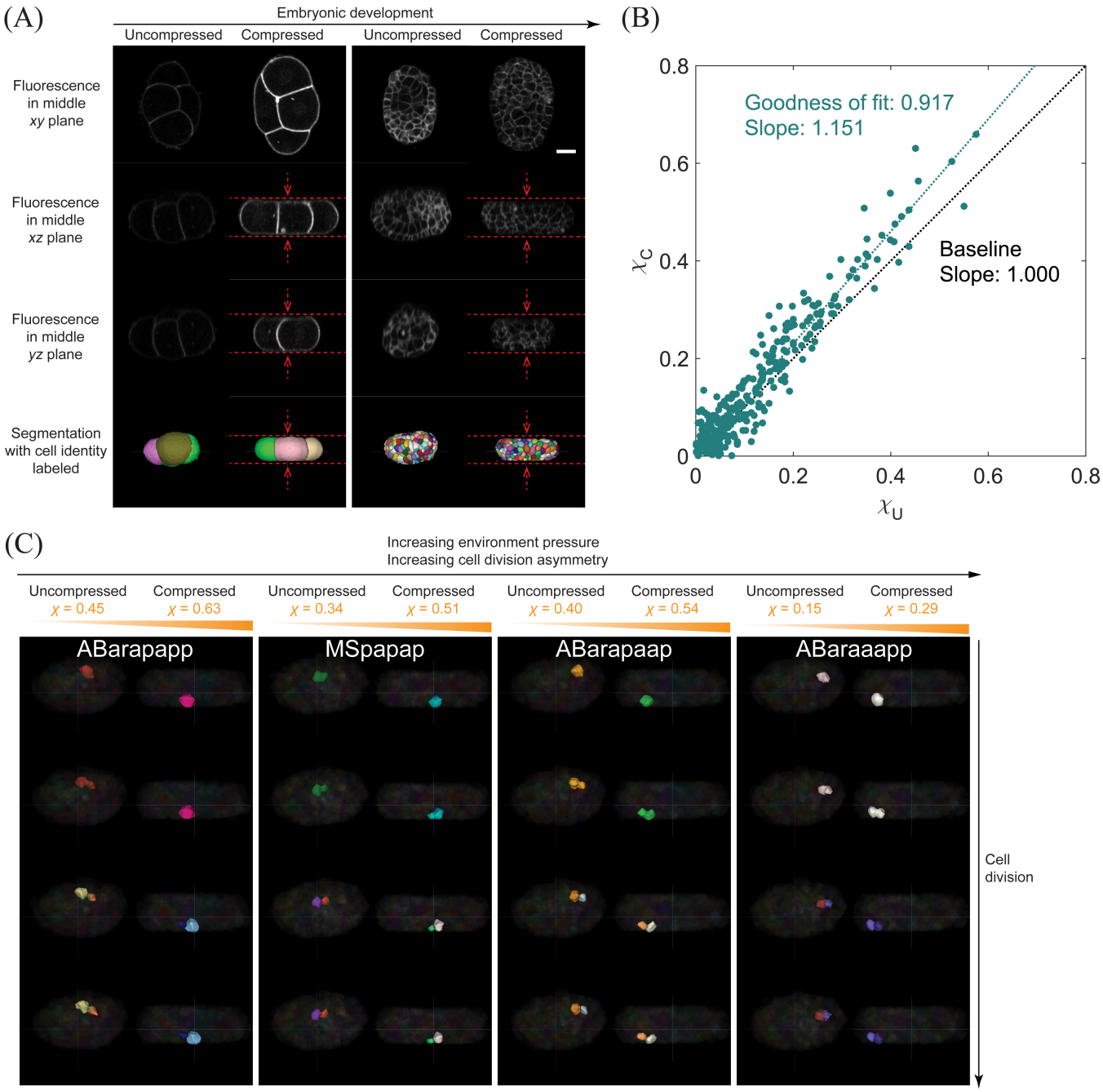


Figure 6. Mechanical confinement amplifies division asymmetry across *C. elegans* embryogenesis. A, Three-dimensional fluorescence imaging of uncompressed (*CMap*) and compressed (*CShaper*) *C. elegans* embryos [29, 30] at an early developmental stage (left two columns, ∼4-cell) and a later stage (right two columns, many-cell), shown in the middle xy, xz, and yz planes (top three rows) and as cell-identity-labeled segmentations (bottom row). Compression visibly flattens the embryo at both stages, reducing the effective shell volume and increasing the confinement parameter ϵ. **B**, Pairwise comparison of division asymmetry between all matched cell division events from uncompressed (χ_U) and compressed (χ_C) embryos. Each point represents one unique cell division; the black dashed line is the identity (slope = 1). Linear regression (green dashed line) yields slope = 1.151 and $R^2 = 0.917$, indicating that compression amplifies χ globally by ∼15% relative to the uncompressed baseline. **C**, Time-lapse images of four representative cell lineages (ABarapapp, MSpapap, ABarapaap, ABaraaapp) under uncompressed and compressed conditions, each shown at multiple successive time points spanning cell division. The asymmetry index χ (annotated above each pair) is consistently higher under compression; the orange bar above each column indicates the direction of increasing division asymmetry.

Methods

Active surface model

We model the cortex as a closed, axisymmetric viscous surface $\mathbf{X}(u,\phi,t)$ (surface coordinates $u \in [0,1]$, $\phi \in [0,2\pi]$), characterized by its metric g_{ij} and curvature tensor C_{ij}, with bending elasticity described by the Helfrich energy [39,40] and shape evolving with the cortical velocity field $\mathbf{v}$ as $d\mathbf{X}/dt = \mathbf{v}$ [18]. Full geometric conventions are given in the Supplementary Information.

The cortical flows are governed by the force balance equation

$$\mathrm{div}(\mathbf{T}) = -\mathbf{f}^{\mathrm{ext}}, \tag{3}$$

where $\mathrm{div}(\cdot) = \mathbf{e}^i \cdot \partial_i(\cdot)$ is the surface divergence operator, $\mathbf{T}$ is the total surface stress tensor, and $\mathbf{f}^{\mathrm{ext}}$ comprises intracellular pressure, frictional drag with the cytoplasm, and normal forces from the confining shell. The intracellular pressure p enters as a Lagrange multiplier that enforces conservation of the cell volume V_{cell} throughout the deformation. We solve for the instantaneous shape $\mathbf{X}$ and flow $\mathbf{v}$ using the variational framework developed in our previous work, in which stationarity of the Rayleigh dissipation functional yields the governing equations [19] (Supplementary Information).

The stress tensor $\mathbf{T}$ decomposes into equilibrium and dissipative contributions. The equilibrium part arises from the Helfrich bending energy $\mathcal{F}_H = \int dA\big[\gamma + \frac{\kappa}{2}(C_k^k)^2\big]$, which penalizes curvature deformations and sets the mechanical stiffness of the cortex. Varying $\mathcal{F}_H$ with respect to surface deformations yields the equilibrium in-plane and normal tension components

$$t_{ij}^H = \gamma g_{ij} + \frac{\kappa}{2} C_k^k \big(C_k^k g_{ij} - 2C_{ij}\big), \qquad t_{i,n}^H = \kappa \nabla_i C_k^k, \tag{4}$$

where γ is the isotropic surface tension and κ the bending rigidity. The dissipative contributions arise from viscous cortical flows and from the active stresses generated by myosin motors [41,42], and the dissipative stress tensor reads

$$t_{ij}^d = 2\eta_s \tilde{S}_{ij} + \eta_b \,\mathrm{div}(\mathbf{v})\, g_{ij} + t_{ij}^a, \tag{5}$$

where η_s and η_b are the surface shear and bulk viscosities, $\tilde{S}_{ij} = S_{ij} - \frac{1}{2} S_k^k g_{ij}$ is the traceless strain-rate tensor, and t_{ij}^a is the curvature-dependent active stress of Eq. (1).

Relation to active thin-shell theory

Modelling the cortex as an elastic shell of finite thickness h, an active stress profile $\zeta_a(z)$ that varies across the shell cross-section generates, upon integration through the thickness, both an active tension $t_a \propto \zeta_a(0)h$, proportional to the mean active stress, and an active bending moment $m_a \propto h^3 \partial_z \zeta_a|_{z=0}$, proportional to the stress gradient [20]. In a curved shell an active bending moment produces an effective in-plane stress proportional to the local curvature [20], yielding a curvature-dependent active tension at the two-dimensional level. A stronger transverse gradient, arising for instance from preferential binding of myosin to the inner face of the actin network, produces a larger active bending moment and hence stronger curvature coupling.

Nondimensionalization and control parameters

We nondimensionalize the model parameters using the bending rigidity κ_0 as the energy scale and the hydrodynamic length $L_h = \sqrt{\eta_b/\Gamma}$, set by the bulk viscosity η_b and the substrate friction Γ, as the length scale, with the corresponding time scale $\tau_\eta = \eta_b L_h^2/\kappa_0$. This yields the dimensionless active couplings $\tilde{\xi}_s = \xi_s \Delta\mu\, L_h/\kappa_0$ and $\tilde{\xi}_b = \xi_b \Delta\mu\, L_h/\kappa_0$. Cell size is measured by the reduced mother-cell radius $\tilde{R}_0 = R_0/L_h$, where R_0 is defined by the cell volume $V_{\mathrm{cell}} = \frac{4\pi}{3} R_0^3$, and the degree of confinement by $\epsilon = V_{\mathrm{cell}}/V_{\mathrm{shell}}$, where V_{shell} is the volume of the ellipsoidal shell. The shared parameter set used throughout is listed in Supplementary Table S3.

Numerical methods

The time derivatives in the dynamic equations are discretized with an implicit finite-difference scheme, so that each time step reduces to a boundary value problem on $u \in [0,1]$. The resulting problems are solved with the MATLAB collocation solver `bvp5c` [43], using relative and absolute tolerances of 10^{-5} and 10^{-8} and a maximum mesh size of 5×10^4. Stationary shapes are obtained by setting the time derivatives to zero and following the solution branches with numerical continuation in $\tilde{\xi}_s$ at fixed coupling ratio. Near a fold, where continuation in activity ceases to be

single-valued, the total meridional arclength is used as the continuation coordinate and the activity is solved for as an additional unknown, which allows both sides of the turning point to be followed.

To probe the sensitivity of the outcome to the initial condition, a small random perturbation is applied to the active couplings at the first time step only: $\tilde{\xi}_s$ and $\tilde{\xi}_b$ are each augmented by $\sum_{n=1}^{10} c_n \cos(n\pi u)$, with the coefficients c_n drawn independently from a uniform distribution on $[-10^{-3}\tilde{\xi}, 10^{-3}\tilde{\xi}]$, where $\tilde{\xi}$ denotes the coupling being perturbed. Each data point with error bars is obtained from ten independent realizations, and the error bars report the resulting standard deviation. The stability of a stationary state is classified dynamically: the state is taken as the initial condition, perturbed as above, and evolved for $40\,\tau_\eta$, and the state is stable when the distance between the time-dependent and stationary shapes decays and unstable when it grows (Supplementary Fig. S5). A division is counted as complete once the furrow radius falls below the numerical cutoff $0.001\,R_0$. Full derivations, boundary conditions, and the definition of the distance function are given in the Supplementary Information.

Experimental data analysis and statistics

We analysed two published cell-resolved four-dimensional morphological datasets of *C. elegans* embryogenesis: *CMap*, comprising eight mechanically uncompressed embryos, and *CShaper*, comprising seventeen mechanically compressed embryos [29, 30]. For each cell identity the segmented volume is averaged over the cell lifespan, and the division asymmetry index $\chi = (V_b - V_s)/(V_b + V_s)$ is computed from the two daughter volumes, where V_b and V_s are the larger and smaller daughter. The statistical unit is therefore a single lineage-resolved division event in a single embryo, and every embryo contributes one value of χ per division event.

For the cell-size analysis, somatic cell division events from the uncompressed dataset are grouped into four mother-cell-volume intervals (10^1–10^2, 10^2–10^3, 10^3–10^4 and 10^4–10^5 μm^3), and adjacent volume groups are compared with a one-sided Wilcoxon rank-sum test. Germline cell division events are compared between adjacent events with the same test. The one-sided form is used because the model predicts the direction of the effect in advance. Significance is annotated as n.s. for $p > 0.1$, one asterisk for $p < 0.1$, two for $p < 0.05$ and three for $p < 0.001$. In the box plots, the box spans the first to third quartiles, the central line marks the median, the whiskers extend to the most extreme values within $[Q_1 - 3\,\mathrm{IQR}, Q_3 + 3\,\mathrm{IQR}]$, where $\mathrm{IQR} = Q_3 - Q_1$ is the interquartile range, and values outside this range are plotted individually. For the confinement comparison, division events are matched between datasets by lineage identity and the matched values are fitted by linear regression, giving a slope of 1.151 with $R^2 = 0.917$. Simulated and segmented cortex contours are compared through the similarity index $|A \cap B|/|A|$, where A and B are the sets of pixels enclosed by the experimental and simulated contours.

Data availability

The data that support the findings of this study are available at `https://github.com/ruima86/AsymmetricCellDivision`.

Code availability

The code used to produce the simulation data in this paper is available from the project repository: `https://github.com/ruima86/AsymmetricCellDivision`.

Acknowledgments

We gratefully acknowledge all members of Tang Lab and Ma Lab, with special thanks to Prof. Xiaojing Yang for insightful discussion. We thank Prof. Fan Jin for critical reading of our manuscript. This work was supported by the Fundamental Research Funds for Central Universities of China under Grant No. 20720250069 to R.M. and the National Natural Science Foundation of China under Grant No. 12474199 to R.M., Grant No. 12090053 to C.T., and Grant No. 32088101 to C.T. and G.G. The authors used AI-based tools to improve the language and readability of the manuscript and to assist in preparing the schematic illustration shown in the inset of Fig. 1A. No experimental image or measured data was generated or altered by such tools. All content was subsequently reviewed and verified by the authors, who take full responsibility for it.

References

1. Guillaume Salbreux, Guillaume Charras, and Ewa Paluch. Actin cortex mechanics and cellular morphogenesis. *Trends in Cell Biology*, 22(10):536–545, 2012.

2. Thomas D Pollard and Gary G Borisy. Cellular motility driven by assembly and disassembly of actin filaments. *Cell*, 112(4):453–465, 2003.

3. Priyamvada Chugh, Andrew G Clark, Matthew B Smith, Davide AD Cassani, Kai Dierkes, Anan Ragab, Philippe P Roux, Guillaume Charras, Guillaume Salbreux, and Ewa K Paluch. Actin cortex architecture regulates cell surface tension. *Nature Cell Biology*, 19(6):689–697, 2017.

4. Ralph A Neumüller and Juergen A Knoblich. Dividing cellular asymmetry: asymmetric cell division and its implications for stem cells and cancer. *Genes & Development*, 23(23):2675–2699, 2009.

5. Subhas Mukherjee, Jun Kong, and Daniel J Brat. Cancer stem cell division: when the rules of asymmetry are broken. *Stem Cells and Development*, 24(4):405–416, 2015.

6. Radek Jankele, Rob Jelier, and Pierre Gönczy. Physically asymmetric division of the *C. elegans* zygote ensures invariably successful embryogenesis. *eLife*, 10:e61714, feb 2021.

7. Yukinobu Arata, Jen-Yi Lee, Bob Goldstein, and Hitoshi Sawa. Extracellular control of PAR protein localization during asymmetric cell division in the C. elegans embryo. *Development*, 137(19):3337–3345, 2010.

8. Rolf Fickentscher, Philipp Struntz, and Matthias Weiss. Setting the clock for fail-safe early embryogenesis. *Physical Review Letters*, 117:188101, 2016.

9. James A. Powers. Live-cell imaging of mitosis in Caenorhabditis elegans embryos. *Methods*, 51(2):197–205, 2010. Methods Related to Mitotic Spindle Research.

10. Kenneth J. Kemphues, James R. Priess, Diane G. Morton, and Niansheng Cheng. Identification of genes required for cytoplasmic localization in early C. elegans embryos. *Cell*, 52(3):311–320, 1988.

11. Nathan W. Goehring, Philipp Khuc Trong, Justin S. Bois, Debanjan Chowdhury, Ernesto M. Nicola, Anthony A. Hyman, and Stephan W. Grill. Polarization of PAR proteins by advective triggering of a pattern-forming system. *Science*, 334(6059):1137–1141, 2011.

12. Anne Sailer, Alexander Anneken, Younan Li, Sam Lee, and Edwin Munro. Dynamic opposition of clustered proteins stabilizes cortical polarity in the C. elegans zygote. *Developmental Cell*, 35(1):131–142, 2015.

13. Rolf Fickentscher, Philipp Struntz, and Matthias Weiss. Mechanical cues in the early embryogenesis of Caenorhabditis elegans. *Biophysical Journal*, 105(8):1805–1811, 2013.

14. Binghui Tian, Guoye Guan, Lei-Han Tang, and Chao Tang. Why and how the nematode's early embryogenesis can be precise and robust: a mechanical perspective. *Physical Biology*, 17:026001, 2020.

15. Hervé Turlier, Basile Audoly, Jacques Prost, and Jean-François Joanny. Furrow constriction in animal cell cytokinesis. *Biophysical Journal*, 106(1):114–123, 2014.

16. Frank Jülicher, Stephan W Grill, and Guillaume Salbreux. Hydrodynamic theory of active matter. *Reports on Progress in Physics*, 81(7):076601, 2018.

17. Guillaume Salbreux and Frank Jülicher. Mechanics of active surfaces. *Physical Review E*, 96(3):032404, 2017.

18. Alexander Mietke, Frank Jülicher, and Ivo F Sbalzarini. Self-organized shape dynamics of active surfaces. *Proceedings of the National Academy of Sciences*, 116(1):29–34, 2019.

19. Da Gao, Huayang Sun, Rui Ma, and Alexander Mietke. Self-organized dynamics and emergent shape spaces of active isotropic fluid surfaces. *Physical Review Research*, 8:023046, Apr 2026.

20. Hélène Berthoumieux, Jean-Léon Maître, Carl-Philipp Heisenberg, Ewa K Paluch, Frank Jülicher, and Guillaume Salbreux. Active elastic thin shell theory for cellular deformations. *New Journal of Physics*, 16:065005, 2014.

21. G. Salbreux, J. Prost, and J. F. Joanny. Hydrodynamics of cellular cortical flows and the formation of contractile rings. *Physical Review Letters*, 103:058102, Jul 2009.

22. Edwin Munro, Jeremy Nance, and James R. Priess. Cortical flows powered by asymmetrical contraction transport PAR proteins to establish and maintain anterior-posterior polarity in the early C. elegans embryo. *Developmental Cell*, 7(3):413–424, 2004.

23. Anne-Cecile Reymann, Fabio Staniscia, Anna Erzberger, Guillaume Salbreux, and Stephan W Grill. Cortical flow aligns actin filaments to form a furrow. *eLife*, 5:e17807, 2016.

24. Shawn N. Jordan, Tim Davies, Yelena Zhuravlev, Julien Dumont, Mimi Shirasu-Hiza, and Julie C. Canman. Cortical PAR polarity proteins promote robust cytokinesis during asymmetric cell division. *Journal of Cell Biology*, 212(1):39–49, 01 2016.

25. Kazunori Yamamoto and Akatsuki Kimura. An asymmetric attraction model for the diversity and robustness of cell arrangement in nematodes. *Development*, 144(23):4437–4449, 2017.

26. Alexander Kirillov, Eric Mintun, Nikhila Ravi, Hanzi Mao, Chloe Rolland, Laura Gustafson, Tete Xiao, Spencer Whitehead, Alexander C. Berg, Wan-Yen Lo, Piotr Dollár, and Ross Girshick. Segment anything. In *2023 IEEE/CVF International Conference on Computer Vision (ICCV)*, pages 3992–4003, 2023.

27. J.E. Sulston and H.R. Horvitz. Post-embryonic cell lineages of the nematode, Caenorhabditis elegans. *Developmental Biology*, 56(1):110–156, 1977.

28. J.E. Sulston, E. Schierenberg, J.G. White, and J.N. Thomson. The embryonic cell lineage of the nematode Caenorhabditis elegans. *Developmental Biology*, 100(1):64–119, 1983.

29. Guoye Guan, Zelin Li, Yiming Ma, Patch Ye, Jianfeng Cao, Ming-Kin Wong, Vincy Ho, Lu Yan Chan, Hong Yan, Chao Tang, and Zhongying Zhao. Cell lineage-resolved embryonic morphological map reveals signaling associated with cell fate and size asymmetry. *Nature Communications*, 16, 04 2025.

30. Jianfeng Cao, Guoye Guan, Vincy Wing Sze Ho, Ming-Kin Wong, Lu-Yan Chan, Chao Tang, Zhongying Zhao, and Hong Yan. Establishment of a morphological atlas of the Caenorhabditis elegans embryo using deep-learning-based 4d segmentation. *Nature Communications*, 11(1):6254, 2020.

31. Filipe Tostevin and Martin Howard. Modeling the establishment of PAR protein polarity in the one-cell C. elegans embryo. *Biophysical Journal*, 95(10):4512–4522, 2008.

32. Yen Wei Lim, Fu-Lai Wen, Prabhat Shankar, Tatsuo Shibata, and Fumio Motegi. A balance between antagonizing PAR proteins specifies the pattern of asymmetric and symmetric divisions in C. elegans embryogenesis. *Cell Reports*, 36(1):109326, 2021.

33. Sungrim Seirin-Lee, Kazunori Yamamoto, and Akatsuki Kimura. The extra-embryonic space and the local contour are crucial geometric constraints regulating cell arrangement. *Development*, 149(9):dev200401, 2022.

34. Jiao Miao, Guoye Guan, and Chao Tang. Spontaneous mechanical and energetic state transitions during Caenorhabditis elegans gastrulation. *arXiv preprint arXiv:2105.05795*, 2021.

35. Sacha Ichbiah, Fabrice Delbary, Alex McDougall, Rémi Dumollard, and Hervé Turlier. Embryo mechanics cartography: inference of 3D force atlases from fluorescence microscopy. *Nature Methods*, 20(12):1989–1999, 2023.

36. Casper van Bavel, Wim Thiels, and Rob Jelier. Cell shape characterization, alignment, and comparison using FlowShape. *Bioinformatics*, 39(6):btad383, 2023.

37. Xiangyu Kuang, Guoye Guan, Chao Tang, and Lei Zhang. MorphoSim: an efficient and scalable phase-field framework for accurately simulating multicellular morphologies. *npj Systems Biology and Applications*, 9:6, 2023.

38. Xiangyu Kuang, Guoye Guan, Ming-Kin Wong, Lu-Yan Chan, Zhongying Zhao, Chao Tang, and Lei Zhang. Computable early Caenorhabditis elegans embryo with a phase field model. *PLoS Computational Biology*, 18(1):1–32, 2022.

39. W Helfrich. Elastic properties of lipid bilayers: theory and possible experiments. *Zeitschrift für Naturforschung. Teil C: Biochemie, Biophysik, Biologie, Virologie*, 28(11):693–703, 1973.

40. Ou-Yang Zhong-can and W. Helfrich. Instability and deformation of a spherical vesicle by pressure. *Physical Review Letters*, 59:2486–2488, Nov 1987.

41. Frank Jülicher, Armand Ajdari, and Jacques Prost. Modeling molecular motors. *Reviews of Modern Physics*, 69:1269–1282, Oct 1997.

42. J. Prost, F. Jülicher, and J. F. Joanny. Active gel physics. *Nature Physics*, 11(2):111–117, 2015.

43. Jacek Kierzenka and Lawrence F. Shampine. A BVP solver based on residual control and the MATLAB PSE. *ACM Transactions on Mathematical Software*, 27(3):299–316, 2001.

44. Amaresh Sahu, Yannick A.D. Omar, Roger A. Sauer, and Kranthi K. Mandadapu. Arbitrary Lagrangian–Eulerian finite element method for curved and deforming surfaces: I. general theory and application to fluid interfaces. *Journal of Computational Physics*, 407:109253, 2020.

45. Udo Seifert, Karin Berndl, and Reinhard Lipowsky. Shape transformations of vesicles: Phase diagram for spontaneous- curvature and bilayer-coupling models. *Physical Review A*, 44:1182–1202, Jul 1991.

Supplementary Information

Cell size and confinement drive asymmetric cell division through a cortical instability

Da Gao, Guoye Guan, Chao Tang and Rui Ma

Contents

Supplementary Note 1: Active-surface model **18**
1.1 Surface geometry and kinematics . . . 18
1.2 Vector and tensor divergence . . . 18
1.3 Passive, viscous, and curvature-dependent active stresses . . . 19
1.4 Confinement, volume constraint, and polarity regulation . . . 19

Supplementary Note 2: Variational formulation **20**
2.1 Rayleigh dissipation functional . . . 20
2.2 Free energy change rate . . . 20
2.3 Entropy production . . . 21
2.4 Enforcing geometric relations via Lagrange multipliers . . . 22
2.5 Force balance from stationarity . . . 22

Supplementary Note 3: Numerical methods and bifurcation analysis **23**
3.1 Boundary conditions from variations . . . 23
3.2 Formulation of boundary value problems . . . 23
3.3 Numerical continuation and stability classification . . . 24
3.4 Division observables and outcome classification . . . 24
3.5 Random perturbation of the initial state . . . 25

Supplementary Note 4: Experimental data analysis **25**
4.1 Embryonic morphological datasets . . . 25
4.2 Cell volumes and division asymmetry . . . 25
4.3 Compression comparison . . . 25
4.4 Cortex-contour comparison and lineage simulation . . . 26

Supplementary Tables **27**

Supplementary Figures **28**

Supplementary Movie Legends **33**

Supplementary Note 1: Active-surface model

We use the active-surface formulation introduced in ref. [19], with the curvature-dependent active stress, confining shell, and localized polarity regulation specified below.

1.1 Surface geometry and kinematics

The geometry and force conventions are summarized in Supplementary Fig. S1. We consider a deforming axisymmetric surface described by

$$\mathbf{X}(u,\phi,t) = [r(u,t)\cos\phi, r(u,t)\sin\phi, z(u,t)], \tag{S1}$$

where $r(u,t)$ and $z(u,t)$ denote time-dependent components of points on the surface, and $u \in [0,1]$ and $\phi \in [0,2\pi]$ are time-independent fixed mesh coordinates. The mapping between the mesh coordinate u and the physical arc length s on the deforming surface is given by the kinematic relation $s = h(t)u$. Additionally, the coordinate r and z depend on the geometric tangential angle ψ through the scaling factor $h(t)$

$$r' = h\cos\psi \tag{S2}$$
$$z' = -h\sin\psi. \tag{S3}$$

Given this, the tangent vectors $\mathbf{e}_i = \partial_i\mathbf{X}$ and surface normal $\mathbf{n} = \mathbf{e}_u \times \mathbf{e}_\phi/|\mathbf{e}_u \times \mathbf{e}_\phi|$ are given by

$$\mathbf{e}_u = h\begin{pmatrix}\cos\psi\cos\phi\\ \cos\psi\sin\phi\\ -\sin\psi\end{pmatrix} \quad \mathbf{e}_\phi = r\begin{pmatrix}-\sin\phi\\ \cos\phi\\ 0\end{pmatrix} \quad \mathbf{n} = \begin{pmatrix}\sin\psi\cos\phi\\ \sin\psi\sin\phi\\ \cos\psi\end{pmatrix}. \tag{S4}$$

The metric tensor $g_{ij} = (\partial_i\mathbf{X})\cdot(\partial_j\mathbf{X})$, Levi-Civita tensor $\epsilon_{ij} = \mathbf{n}\cdot(\mathbf{e}_i \times \mathbf{e}_j)$ as well as the curvature tensor $C_{ij} = -\mathbf{n}\cdot\partial_i\partial_j\mathbf{X}$ are diagonal and read

$$g_{ij} = \begin{pmatrix}g_{uu} & 0\\ 0 & g_{\phi\phi}\end{pmatrix} = \begin{pmatrix}h^2 & 0\\ 0 & r^2\end{pmatrix} \tag{S5}$$
$$\epsilon_{ij} = \begin{pmatrix}\epsilon_{uu} & \epsilon_{u\phi}\\ \epsilon_{\phi u} & \epsilon_{\phi\phi}\end{pmatrix} = \sqrt{g}\begin{pmatrix}0 & 1\\ -1 & 0\end{pmatrix} \tag{S6}$$
$$C_{ij} = \begin{pmatrix}C_{uu} & 0\\ 0 & C_{\phi\phi}\end{pmatrix} = \begin{pmatrix}h\psi' & 0\\ 0 & r\sin\psi\end{pmatrix}, \tag{S7}$$

where $g = \det(g_{ij})$.

The surface dynamics are described by the surface velocity field

$$\begin{aligned}\mathbf{v}(u,\phi,t) &= v^u(u,t)\,\mathbf{e}_u + v^\phi(u,t)\,\mathbf{e}_\phi + v_n(u,t)\,\mathbf{n}\\ &= \bar{v}_u(u,t)\,\bar{\mathbf{e}}_u + \bar{v}_\phi(u,t)\,\bar{\mathbf{e}}_\phi + v_n(u,t)\,\mathbf{n}.\end{aligned} \tag{S8}$$

Following the arbitrary Lagrangian–Eulerian (ALE) framework [44], the center-of-mass flow is $\mathbf{v} = d\mathbf{X}/dt$ with material derivative $d/dt = \partial_t + q^u\,\partial_u$, where the coordinate flow q^u accounts for the motion of a surface point relative to the mesh coordinates. This yields

$$q^u = v^u - h^{-1}(\sin\psi\,\partial_t z - \cos\psi\,\partial_t r), \tag{S9}$$
$$v_n = \sin\psi\,\partial_t r + \cos\psi\,\partial_t z. \tag{S10}$$

1.2 Vector and tensor divergence

The surface divergences of a vector field $\mathbf{v}$ and a tension tensor field $\mathbf{T}$ are

$$\mathrm{div}(\mathbf{v}) = \mathbf{e}^i\cdot\partial_i\mathbf{v} = \nabla_i v^i + C^k_k v_n \qquad \mathrm{div}(\mathbf{T}) = \mathbf{e}^i\cdot\partial_i\mathbf{T} = \nabla_i\mathbf{t}^i. \tag{S11}$$

Throughout, we use the normalized tangent basis vectors $\bar{\mathbf{e}}_u := \mathbf{e}_u/h$ and $\bar{\mathbf{e}}_\phi := \mathbf{e}_\phi/r$, with $\mathbf{e}_i$ given in Eqs. (S4), and decompose $\mathbf{v} = \bar{v}_i\bar{\mathbf{e}}_i + v_n\mathbf{n}$ and $\mathbf{T} = \bar{\mathrm{T}}_{ij}\bar{\mathbf{e}}_i\otimes\bar{\mathbf{e}}_j + \bar{\mathrm{T}}_{n,i}\bar{\mathbf{e}}_i\otimes\mathbf{n}$. The explicit component expressions for $\mathrm{div}(\mathbf{v})$ and $\mathrm{div}(\mathbf{T})$ on the axisymmetric surface are given in ref. [19] [Eqs. (S13)–(S16) therein].

1.3 Passive, viscous, and curvature-dependent active stresses

The equilibrium tension and moment tensors arising from the Helfrich free energy $\mathcal{F}_H = \int dA\,[\gamma + \frac{\kappa}{2}(C_k^k)^2]$, the strain-rate tensor $\mathbf{S} = \frac{1}{2}(\mathbf{e}_i \cdot \partial_j \mathbf{v} + \mathbf{e}_j \cdot \partial_i \mathbf{v})\,\mathbf{e}^i \otimes \mathbf{e}^j$ together with its isotropic and traceless parts $\mathbf{S}^{\rm iso}$ and $\tilde{\mathbf{S}}$, and the general force- and torque-balance equations on an axisymmetric surface, are all given in ref. [19] (Secs. IV and V therein) and are used here without modification; the present model has no spontaneous curvature ($C_0 = 0$). On the axisymmetric surface the curvature tensor has components $\bar{C}_{uu} = \psi'/h$ and $\bar{C}_{\phi\phi} = \sin\psi/r$, and its traceless part is

$$\tilde{\mathbf{C}} = \frac{1}{2}\left(\frac{\psi'}{h} - \frac{\sin\psi}{r}\right)(\bar{\mathbf{e}}_u \otimes \bar{\mathbf{e}}_u - \bar{\mathbf{e}}_\phi \otimes \bar{\mathbf{e}}_\phi)\,, \tag{S12}$$

where the prefactor $\psi'/h - \sin\psi/r = C_u^u - C_\phi^\phi$ is the difference between the two principal curvatures.

The modification specific to the present work is the curvature-dependent active stress in the dissipative tension tensor $\mathbf{T}_d$. Instead of the constant isotropic active stress $\propto \xi\Delta\mu$ of ref. [19], the active stress here is linear in the curvature tensor, with a deviatoric contribution $\propto \xi_s\Delta\mu\,\tilde{\mathbf{C}}$ and an isotropic contribution $\propto \xi_b\Delta\mu\,C_k^k\mathbf{G}$ that depends on the mean curvature. On the axisymmetric surface, $\mathbf{T}_d = (\bar{\mathrm{T}}_d)_{uu}\bar{\mathbf{e}}_u \otimes \bar{\mathbf{e}}_u + (\bar{\mathrm{T}}_d)_{\phi\phi}\bar{\mathbf{e}}_\phi \otimes \bar{\mathbf{e}}_\phi + (\bar{\mathrm{T}}_d)_{u\phi}(\bar{\mathbf{e}}_u \otimes \bar{\mathbf{e}}_\phi + \bar{\mathbf{e}}_\phi \otimes \bar{\mathbf{e}}_u)$, with components

$$(\bar{\mathrm{T}}_d)_{uu} = \eta_b(\bar{S}_{uu} + \bar{S}_{\phi\phi}) + \eta_s(\bar{S}_{uu} - \bar{S}_{\phi\phi}) + \frac{1}{2}\xi_s\Delta\mu\left(\bar{C}_{uu} - \bar{C}_{\phi\phi}\right) + \xi_b\Delta\mu(\bar{C}_{uu} + \bar{C}_{\phi\phi}) \tag{S13}$$

$$(\bar{\mathrm{T}}_d)_{\phi\phi} = \eta_b(\bar{S}_{uu} + \bar{S}_{\phi\phi}) - \eta_s(\bar{S}_{uu} - \bar{S}_{\phi\phi}) - \frac{1}{2}\xi_s\Delta\mu\left(\bar{C}_{uu} - \bar{C}_{\phi\phi}\right) + \xi_b\Delta\mu(\bar{C}_{uu} + \bar{C}_{\phi\phi}) \tag{S14}$$

$$(\bar{\mathrm{T}}_d)_{u\phi} = (\bar{T}_d)_{\phi u} = 2\eta_s\bar{S}_{u\phi}, \tag{S15}$$

where the strain-rate components in the normalized basis read [19]

$$\bar{S}_{uu} = \frac{1}{h}\bar{v}_u' + \frac{\psi'}{h}\,v_n, \tag{S16}$$

$$\bar{S}_{\phi\phi} = \frac{\cos\psi}{r}\,\bar{v}_u + \frac{\sin\psi}{r}\,v_n, \tag{S17}$$

$$\bar{S}_{u\phi} = \frac{1}{2}\left(\frac{\bar{v}_\phi'}{h} - \frac{\cos\psi}{r}\,\bar{v}_\phi\right), \tag{S18}$$

with $\bar{v}_u, \bar{v}_\phi$ the tangential flow components in the normalized basis, v_n the normal velocity, and a prime denoting ∂_u. The deviatoric active stress $\xi_s\Delta\mu\,\tilde{\mathbf{C}}$, proportional to the difference between the two principal curvatures, is the major contribution responsible for forming the strongly ingressed cleavage furrow.

The total tension tensor is $\mathbf{T} = \mathbf{T}_e + \mathbf{T}_d$, where $\mathbf{T}_d$ is the dissipative stress and $\mathbf{T}_e$ is the equilibrium (Helfrich) stress,

$$\mathbf{T}_e = t_{ij}^H\,\mathbf{e}^i \otimes \mathbf{e}^j + t_{i,n}^H\,\mathbf{e}^i \otimes \mathbf{n}, \tag{S19}$$

whose components t_{ij}^H and $t_{i,n}^H$ are given in Eq. (4) of the main text. The force balance $\mathrm{div}(\mathbf{T}) = -\mathbf{f}^{\rm ext}$ is given as Eq. (3) in the main text.

1.4 Confinement, volume constraint, and polarity regulation

The cortex is enclosed by an axisymmetric ellipsoidal shell with major and minor semi-axes a and b. Its volume is $V_{\rm shell} = 4\pi ab^2/3$, and the degree of confinement is measured by

$$\epsilon = \frac{V_{\rm cell}}{V_{\rm shell}}, \tag{S20}$$

where $V_{\rm cell} = 4\pi R_0^3/3$ defines the equivalent mother-cell radius R_0. Conservation of $V_{\rm cell}$ is imposed by the pressure difference p, which is solved as a Lagrange multiplier. Contact with the confining shell is represented by the potential

$$P^{\rm ext}(u,\phi,t) = P_0\exp\left[\frac{z^2/a^2 + r^2/b^2 - 1}{w_p^2}\right], \tag{S21}$$

with the corresponding normal force

$$\mathbf{f}^c = f_n^c\mathbf{n} = -\left(\frac{\partial P^{\rm ext}}{\partial r}\sin\psi + \frac{\partial P^{\rm ext}}{\partial z}\cos\psi\right)\mathbf{n}. \tag{S22}$$

For polarity-regulated divisions, the bending rigidity is modulated by a localized Gaussian profile,

$$\kappa(u) = \kappa_0 \left[1 + \Delta_\kappa \exp\left(-\frac{(u-u_0)^2}{\omega^2}\right)\right], \tag{S23}$$

where u_0, ω, and Δ_κ specify the position, width, and amplitude of the cue. Somatic-lineage simulations use a spatially uniform bending rigidity, whereas the P-lineage simulations use the localized profile.

We nondimensionalize lengths by the hydrodynamic length $L_h = \sqrt{\eta_b/\Gamma}$, energies by κ_0, and times by $\tau_\eta = \eta_b L_h^2/\kappa_0$. The resulting control parameters include $\tilde{R}_0 = R_0/L_h$, $\tilde{\xi}_s = \xi_s \Delta\mu L_h/\kappa_0$, and $\tilde{\xi}_b = \xi_b \Delta\mu L_h/\kappa_0$. The shared parameter set used for the lineage calculation is listed in Supplementary Table S3.

Supplementary Note 2: Variational formulation

2.1 Rayleigh dissipation functional

We introduce the Rayleigh dissipation functional $\mathcal{R}$, whose stationary points

$$\frac{\delta \mathcal{R}}{\delta \mathbf{v}} = 0 \tag{S24}$$

have been shown to be equivalent to the force-balance equation, Eq. (3) in the main text (see Ref. [19] for a detailed derivation).

Within the Onsager framework, the Rayleighian is given by the sum of the rate of change of the free energy and the entropy production rate,

$$\mathcal{R}(\mathbf{v}, r_p) = \frac{dF}{dt} + \mathcal{D}, \tag{S25}$$

where dF/dt represents the reversible contribution associated with conservative forces, and $\mathcal{D}$ denotes the dissipation function, which is quadratic in the generalized velocities and encodes irreversible processes. For active surfaces, $\mathcal{D}$ also includes contributions from nonequilibrium driving, such as chemical activity.

In the following, we provide explicit expressions for the free energy change rate dF/dt and the entropy production rate $\mathcal{D}$.

2.2 Free energy change rate

The equilibrium elastic properties of the surface are described by the Helfrich free-energy density $f_H = \gamma_H + f_\kappa$ [39], with passive surface tension γ_H and bending energy density

$$f_\kappa = \frac{1}{2}\kappa \left(C_k^k\right)^2 = \frac{1}{2}\kappa \left(\frac{\psi'}{h} + \frac{\sin\psi}{r}\right)^2 \tag{S26}$$

(the Gaussian-curvature term is omitted, as the surface has spherical topology). The surface is additionally driven out of equilibrium by chemical reactions with chemical free-energy density $f_c(c_f, c_p)$, whose chemical potentials $\mu_n = \partial f_c/\partial c_n$ $(n = f, p)$—corresponding, in biological systems, to the reactants and products of ATP hydrolysis [41, 42]—define the chemical potential difference $\Delta\mu = \mu_f - \mu_p$ that acts as the nonequilibrium driving force generating the active stresses. Finally, a velocity-independent external force $\mathbf{f}_e^{\text{ext}} = p\mathbf{n} + f_n^c \mathbf{n}$ arises from the intracellular pressure p and from the normal force f_n^c exerted by the confining potential [Eq. (S22)].

Applying the surface transport theorem [ref. [19], Eq. (S36) therein] to the elastic, chemical, and external-force contributions yields the total free-energy change rate

$$\frac{dF}{dt} = 2\pi \int_0^1 \left[\partial_t f_\kappa + \frac{f_\kappa}{rh}\,\partial_t(rh) + \gamma\,\mathrm{div}(\mathbf{v}) - r_p\,\Delta\mu + J_n^{\text{ext}} - \mathbf{f}_e^{\text{ext}} \cdot \mathbf{v}\right] rh\,du + 2\pi\,\left(f_\kappa q^u rh\right)\big|_0^1, \tag{S27}$$

where $\gamma = \gamma_e + \gamma_H$ is the total passive tension with effective chemical tension $\gamma_e = f_c - \mu_f c_f - \mu_p c_p$, $r_p = -r_f$ is the production rate of the product species, and $J_n^{\text{ext}} = J_{n,f}\mu_f + J_{n,p}\mu_p$ is the influx of chemical free energy from the environment. We assume J_n^{ext} is such that $\Delta\mu$ is maintained constant in space and time.

2.3 Entropy production

The dissipative part of the Rayleigh functional $\mathcal{D}$ has contributions from the internal and external dissipation, respectively. The internal dissipation is defined as

$$\Theta_{\text{int}} = \int dA \left(\mathbf{T}_d : \mathbf{S} + r_p \Delta\mu \right). \tag{S28}$$

Note that thermodynamic variables ($\mathbf{T}_d$,$\Delta\mu$) are even, while their conjugate partners ($\mathbf{S}$,r_p) are odd under time-reversal. The $\Delta\mu$ is commonly treated as the thermodynamic force [41]. Given this, the thermodynamic flux $\mathbf{T}_d$ is expressed as the constitutive law

$$\mathbf{T}_d = 2\eta_s \tilde{\mathbf{S}} + \eta_b \text{div}(\mathbf{v})\mathbf{G} + \xi_s \Delta\mu \tilde{\mathbf{C}} + \xi_b \Delta\mu C_k^k \mathbf{G}, \tag{S29}$$

as presented in Eq. 5 and the thermodynamic flux r_p is expressed as

$$\begin{aligned} r_p &= -\xi_s \tilde{\mathbf{C}} : \tilde{\mathbf{S}} - 2\xi_b \mathbf{C}^{\text{iso}} : \mathbf{S}^{\text{iso}} + \Lambda \Delta\mu \\ &= -\xi_s \tilde{\mathbf{C}} : \tilde{\mathbf{S}} - \xi_b C_k^k \text{div}(\mathbf{v}) + \Lambda \Delta\mu \end{aligned} \tag{S30}$$

with the phenomenological Onsager coefficients $\eta_s, \eta_b, \Lambda, \xi_s$ and ξ_b. Onsager reciprocity relations require that the reactive coefficients of cross-coupling must adopt opposite signs with ξ_s (ξ_b) and $-\xi_s$ ($-\xi_b$) in the constitutive laws Eqs. (S29) and (S30) [16]. Note that the reactive part ξ_s and ξ_b do not contribute to entropy production and dissipation in non-equilibrium systems. Consequently, it is necessary to introduce a reformulated expression for entropy production that depends exclusively on the dissipative Onsager coefficients. In this context, the chemical production rate r_p is adopted as the thermodynamic force instead of $\Delta\mu$

$$\Delta\hat{\mu} = \frac{\xi_s}{\Lambda} \tilde{\mathbf{C}} : \tilde{\mathbf{S}} + \frac{\xi_b}{\Lambda} C_k^k \text{div}(\mathbf{v}) + \frac{1}{\Lambda} r_p, \tag{S31}$$

the constitutive law corresponding to the thermodynamic flux $\mathbf{T}_d$ reads

$$\begin{aligned} \hat{\mathbf{T}}_d = 2\eta_s \tilde{\mathbf{S}} &+ \left(\eta_b + \frac{\xi_b^2}{\Lambda} \left(C_k^k \right)^2 \right) \text{div}(\mathbf{v})\mathbf{G} + \frac{\xi_s \xi_b}{\Lambda} C_k^k \text{div}(\mathbf{v}) \tilde{\mathbf{C}} + \frac{{\xi_s}^2}{\Lambda} (\tilde{\mathbf{C}} : \tilde{\mathbf{S}}) \tilde{\mathbf{C}} \\ &+ \frac{\xi_b \xi_s}{\Lambda} C_k^k (\tilde{\mathbf{C}} : \tilde{\mathbf{S}}) \mathbf{G} + \frac{\xi_s}{\Lambda} r_p \tilde{\mathbf{C}} + \frac{\xi_b}{\Lambda} C_k^k r_p \mathbf{G}. \end{aligned} \tag{S32}$$

The Onsager coefficients ξ_s/Λ and $\xi_b C_k^k/\Lambda$ now appear as dissipative terms with the same sign in both constitutive laws Eqs. (S31) and (S32) and cross-couples flux-force pairs ($\hat{\mathbf{T}}_d, r_p$) with opposite time-reversal signature. The new internal entropy production $\hat{\Theta}_{\text{int}}$ associated with constitutive laws Eqs. (S31) and (S32) is written as

$$\begin{aligned} \hat{\Theta}_{\text{int}}(\mathbf{v}, r_p) &= \int \left(\hat{\mathbf{T}}_d : \mathbf{S} + r_p \Delta\hat{\mu} \right) dA \\ &= \int (S_1 + S_2 + S_3) dA, \end{aligned} \tag{S33}$$

where

$$\begin{aligned} S_1 &= \eta_b \left(\bar{S}_{uu} + \bar{S}_{\phi\phi} \right)^2 \\ S_2 &= \eta_s \left[\left(\bar{S}_{uu} - \bar{S}_{\phi\phi} \right)^2 + \left(2\bar{S}_{u\phi} \right)^2 \right] \\ S_3 &= \frac{1}{\Lambda} \left[r_p + \xi_b \left(\bar{C}_{uu} + \bar{C}_{\phi\phi} \right) \left(\bar{S}_{uu} + \bar{S}_{\phi\phi} \right) + \frac{\xi_s}{2} \left(\bar{C}_{uu} - \bar{C}_{\phi\phi} \right) \left(\bar{S}_{uu} - \bar{S}_{\phi\phi} \right) \right]^2. \end{aligned} \tag{S34}$$

The external frictional forces introduced in the force-balance equation [Eq. (3) in the main text] will additionally contribute to entropy production in the form

$$\Theta_{\text{ext}} = -\int \mathbf{v} \cdot \mathbf{f}_d^{\text{ext}} dA = 2\pi \int_0^1 \left[\Gamma \bar{v}_u^2 + \Gamma \bar{v}_\phi^2 \right] r h du \tag{S35}$$

where $\mathbf{f}_d^{\text{ext}} = -\Gamma \mathbf{v}_\parallel$ is the tangential frictional force, with $\mathbf{v}_\parallel = \bar{v}_u \bar{\mathbf{e}}_u + \bar{v}_\phi \bar{\mathbf{e}}_\phi$ the in-plane surface velocity. Taking everything into account, the dissipative part of the Rayleigh functional $\mathcal{D}$ is then given by

$$\mathcal{D}(\mathbf{v}, r_p) = \frac{1}{2} \left(\hat{\Theta}_{\text{int}} + \Theta_{\text{ext}} \right). \tag{S36}$$

2.4 Enforcing geometric relations via Lagrange multipliers

To enforce the SLE gauge condition $h' = 0$, as well as the geometric relations that relate r and z to h and ψ, we introduce Lagrange multipliers following the standard approach [45]. The Rayleigh dissipation functional, therefore, acquires additional constraint terms.

$$\mathcal{L} = 2\pi \int_0^1 du\, \partial_t [\alpha\,(r' - h\cos\psi) + \beta\,(z' + h\sin\psi) + \zeta\, h']\,, \tag{S37}$$

where α, β, and ζ are Lagrange multipliers enforcing the corresponding geometric constraints.

Collecting all contributions, the final constrained Rayleigh dissipation functional reads

$$\begin{aligned}\bar{\mathcal{R}} &= \mathcal{R} + \mathcal{L} \\ &= 2\pi \int_0^1 \Bigg[\partial_t f_\kappa + f_\kappa \frac{\partial_t (rh)}{rh} - r_p\,\Delta\mu - \mathbf{f}_e^{\text{ext}}\cdot\mathbf{v} + \gamma\,\text{div}(\mathbf{v}) + \frac{1}{2}\,(S_1 + S_2 + S_3) + \frac{1}{2}\Gamma\left(\bar{v}_u^2 + \bar{v}_\phi^2\right) \\ &\quad + J_n^{\text{ext}}\Bigg] rh\, du + 2\pi \int_0^1 du\, \partial_t [\alpha\,(r' - h\cos\psi) + \beta\,(z' + h\sin\psi) + \zeta\, h'] + 2\pi\,\left(f_\kappa q^u rh\right)\big|_0^1\,.\end{aligned} \tag{S38}$$

Here $\mathcal{R}$ and $\mathcal{L}$ are defined in Eqs. (S25) and (S37), respectively. The velocity-independent external force is purely normal, $\mathbf{f}_e^{\text{ext}} = f_n^{\text{ext}}\mathbf{n}$, and enters the Rayleighian only through the term $-\mathbf{f}_e^{\text{ext}}\cdot\mathbf{v} = -f_n^{\text{ext}} v_n$ in Eq. (S38). The tangential frictional force is not part of $\mathbf{f}_e^{\text{ext}}$ and is instead represented by the dissipation term $\frac{1}{2}\Gamma(\bar{v}_u^2 + \bar{v}_\phi^2)$. Specific to the present work is the normal external force, with

$$f_n^{\text{ext}} = p + f_n^c, \tag{S39}$$

which includes the pressure difference p that enforces conservation of the enclosed volume and the confinement force f_n^c defined from Eq. (S21).

In the following, the constrained Rayleigh dissipation functional $\bar{\mathcal{R}}$ is varied with respect to the generalized variables

$$\Phi \in \left\{v^u,\, v^\phi,\, \partial_t r,\, \partial_t z,\, \partial_t h,\, \partial_t \psi,\, \partial_t \alpha,, \partial_t \beta,\, \partial_t \zeta\right\},$$

by imposing the stationarity condition

$$\frac{\delta \bar{\mathcal{R}}}{\delta \Phi} = 0. \tag{S40}$$

2.5 Force balance from stationarity

The density of the unconstrained Rayleighian $\mathcal{R}(\mathbf{v}, r_p)$ [Eq. (S25)] reads

$$\begin{aligned}R(\mathbf{v}, r_p) = \Bigg[&\partial_t f_\kappa + f_\kappa \frac{\partial_t (rh)}{rh} - r_p \Delta\mu + J_n^{\text{ext}} - \mathbf{f}_e^{\text{ext}}\cdot\mathbf{v} + \gamma \text{div}(\mathbf{v}) \\ &+ \frac{1}{2}(S_1 + S_2 + S_3) + \frac{1}{2}\Gamma\left(\bar{v}_u^2 + \bar{v}_\phi^2\right)\Bigg] rh,\end{aligned} \tag{S41}$$

with f_κ given in Eq. (S26) and $(S_1 + S_2 + S_3)$ given in Eq. (S34). The density of the constrained functional $\bar{\mathcal{R}}$ [Eq. (S38)] additionally includes the Lagrange-multiplier terms,

$$\bar{R} = R(\mathbf{v}, r_p) + \partial_t \left[\alpha(r' - h\cos\psi) + \beta(z' + h\sin\psi) + \zeta h'\right]. \tag{S42}$$

Following the same variational procedure as ref. [19], the stationarity conditions $\delta\bar{\mathcal{R}}/\delta\Phi = 0$ [Eq. (S40)] reproduce the force-balance equations of the active surface; we summarize the resulting equations below and refer to ref. [19] for the detailed algebra.

The variation with respect to the reaction rate, $\delta\bar{\mathcal{R}}/\delta r_p = 0$, gives

$$\frac{1}{\Lambda}\left[r_p + \xi_b\left(\bar{C}_{uu} + \bar{C}_{\phi\phi}\right)\left(\bar{S}_{uu} + \bar{S}_{\phi\phi}\right) + \frac{\xi_s}{2}\left(\bar{C}_{uu} - \bar{C}_{\phi\phi}\right)\left(\bar{S}_{uu} - \bar{S}_{\phi\phi}\right)\right] - \Delta\mu = 0, \tag{S43}$$

from which the constitutive law for the production rate r_p [Eq. (S31)] follows. Variations with respect to the tangential flows $\bar{v}_u$ and $\bar{v}_\phi$ reproduce the meridional and azimuthal components of the tangential force balance. The production

rate r_p arising from these variations is replaced by $\Delta\mu$ through Eq. (S43), so that the dissipative stress enters in its $\Delta\mu$ form $\mathbf{T}_d$,

$$\bar{\mathbf{e}}_u \cdot \mathrm{div}(\mathbf{T}_d + \mathbf{T}_e) = \Gamma \bar{v}_u - f_u^{\mathrm{ext}}, \tag{S44}$$

$$\bar{\mathbf{e}}_\phi \cdot \mathrm{div}(\mathbf{T}_d + \mathbf{T}_e) = \Gamma \bar{v}_\phi - f_\phi^{\mathrm{ext}}. \tag{S45}$$

Variations with respect to $\partial_t r$, $\partial_t z$, $\partial_t \psi$ and $\partial_t h$, together with the geometric relations imposed through the Lagrange multipliers α, β and ζ, reproduce the normal force balance. As in ref. [19], the boundary term of the h variation enforces $\zeta(0) = \zeta(1) = 0$, which together with $\zeta'' = 0$ yields $\zeta = 0$; eliminating α and β then leads to

$$\mathbf{n} \cdot \mathrm{div}(\mathbf{T}_d + \mathbf{T}_e) = -f_n^{\mathrm{ext}}. \tag{S46}$$

As in the tangential components, the production rate r_p arising from the variation is replaced by $\Delta\mu$ through Eq. (S43), so that all three force-balance equations use the same dissipative stress $\mathbf{T}_d$. In these variational force-balance equations, the dissipative stress $\mathbf{T}_d$ and the friction force $\Gamma\mathbf{v}$ arise from variations of the dissipation rate $\mathcal{D}$, while the equilibrium stress $\mathbf{T}_e$ and the velocity-independent external force $\mathbf{f}^{\mathrm{ext}}$ arise from variations of the free-energy change rate dF/dt.

Supplementary Note 3: Numerical methods and bifurcation analysis

3.1 Boundary conditions from variations

The variations Eq. (S40) generate the boundary conditions including

$$\left[\frac{\partial \bar{R}}{\partial[(\bar{v}_u)']} + \frac{\partial(f_\kappa q^u r h)}{\partial \bar{v}_u}\right] \delta\bar{v}_u \Big|_{u=0}^{u=1} = r\bar{\mathbf{e}}_u \cdot [(f_\kappa + \gamma)\mathbf{G} + \mathbf{T}_d] \cdot \bar{\mathbf{e}}_u \delta\bar{v}_u \Big|_{u=0}^{u=1} \tag{S47}$$

$$\frac{\partial \bar{R}}{\partial[(\bar{v}_\phi)']} \delta\bar{v}_\phi \Big|_{u=0}^{u=1} = r\bar{\mathbf{e}}_u \cdot [(f_\kappa + \gamma)\mathbf{G} + \mathbf{T}_d] \cdot \bar{\mathbf{e}}_\phi \delta\bar{v}_\phi \Big|_{u=0}^{u=1} \tag{S48}$$

$$\left[\frac{\partial \bar{R}}{\partial[(\partial_t r)']} + \frac{\partial(f_\kappa q^u r h)}{\partial(\partial_t r)}\right] \delta(\partial_t r) \Big|_{u=0}^{u=1} = (\alpha - f_\kappa r \cos\psi)\delta(\partial_t r) \Big|_{u=0}^{u=1} \tag{S49}$$

$$\left[\frac{\partial \bar{R}}{\partial[(\partial_t z)']} + \frac{\partial(f_\kappa q^u r h)}{\partial(\partial_t z)}\right] \delta(\partial_t z) \Big|_{u=0}^{u=1} = (\beta + f_\kappa r \sin\psi)\delta(\partial_t z) \Big|_{u=0}^{u=1} \tag{S50}$$

$$\frac{\partial \bar{R}}{\partial[(\partial_t \psi)']} \delta(\partial_t \psi) \Big|_{u=0}^{u=1} = r\,\bar{\mathbf{e}}_u \cdot \mathbf{M}_e \cdot \bar{\mathbf{e}}_\phi \delta(\partial_t \psi) \Big|_{u=0}^{u=1}, \tag{S51}$$

where the equilibrium moment $\mathbf{M}_e = (\bar{M}_e)_{ij}\bar{\mathbf{e}}_i \otimes \bar{\mathbf{e}}_j$, the metric tensor $\mathbf{G} = \bar{\mathbf{e}}_u \otimes \bar{\mathbf{e}}_u + \bar{\mathbf{e}}_\phi \otimes \bar{\mathbf{e}}_\phi$, and the dissipative tension $\mathbf{T}_d = (\bar{\mathrm{T}}_d)_{ij}\bar{\mathbf{e}}_i \otimes \bar{\mathbf{e}}_j$. The boundary conditions are summarized in Tab. S2.

3.2 Formulation of boundary value problems

In the ODE system summarized in Tab. S1, all equations are formulated as functions of the meridional coordinate u. To compute time-dependent solutions, the time derivatives $\partial_t r$, $\partial_t z$, and $\partial_t \psi$ appearing in these equations are discretized using a finite difference scheme, thereby eliminating explicit derivatives with respect to t. After this temporal discretization, the governing equations reduce to a boundary value problem (BVP) defined on the fixed interval $u \in [0, 1]$. For the dynamic equations, we set

$$\begin{aligned} \partial_t r &= \frac{r(u,t) - r(u,t-\Delta t)}{\Delta t} \\ \partial_t z &= \frac{z(u,t) - z(u,t-\Delta t)}{\Delta t} \\ \partial_t \psi &= \frac{\psi(u,t) - \psi(u,t-\Delta t)}{\Delta t}, \end{aligned} \tag{S52}$$

and using $r(u, t-\Delta t), z(u, t-\Delta t), \psi(u, t-\Delta t)$ from the previous time-step. This represents an implicit scheme to numerically integrate the equations. Solutions $[r(u,t), z(u,t), \psi(u,t), v_u, v_\phi]$ of the ODE system derived from the variational formulation then directly correspond to the surface geometries and flows at the next time point. Tab. S1

provides nine equations that are equivalent to twelve first-order ODEs. To enforce volume conservation, we introduce the auxiliary volume function $V(u)$, which satisfies

$$V' = \pi r^2 h \sin\psi, \tag{S53}$$

together with the boundary conditions

$$V(0) = 0, \qquad V(1) = V_{\mathrm{cell}} = \frac{4\pi}{3} R_0^3. \tag{S54}$$

Combining Eq. (S53) with the ODEs listed in Tab. S1 yields a total of thirteen first-order ODEs. Tab. S2 specifies twelve boundary conditions; together with Eq. (S54), there are fourteen boundary conditions in total. Including the additional unknown Lagrange multiplier p that enforces volume conservation, these ODEs and boundary conditions constitute a well-posed BVP. We solve this problem using standard BVP solvers implemented in MATLAB [43].

3.3 Numerical continuation and stability classification

Stationary shapes are obtained by setting the time derivatives in the dynamic equations to zero and solving the resulting BVP. We first construct a passive reference shape at zero activity and then follow the solution as the active couplings are varied, using each converged solution as the initial guess for the neighboring parameter value. The ratio between the two active couplings is held fixed while $\tilde{\xi}_s$ is used as the activity coordinate. Near a fold, where direct activity continuation ceases to be single-valued, the total meridional arclength is prescribed as the continuation coordinate and the active strength is solved as an additional unknown. This procedure allows both sides of the turning point to be followed and produces the stationary branches shown in Fig. 2 of the main text and Supplementary Fig. S4.

The stationary BVPs are solved with MATLAB's collocation solver `bvp5c`, using relative and absolute tolerances of 10^{-5} and 10^{-8}, respectively, and a maximum mesh size of 5×10^4. Mirror-symmetric branches are initialized from equatorially symmetric profiles. Symmetry-broken branches are obtained by seeding the stationary solver with a small antisymmetric displacement. Local stability of a stationary solution is assessed dynamically. Denoting the stationary shape by $[r_0(u), z_0(u)]$, we take it as the initial condition, add the small random perturbation described in Sec. 3.5, and evolve the time-dependent equations. Writing the evolving shape as $[r(u,t), z(u,t)]$, we monitor its distance from the stationary state,

$$\mathrm{dis}(t) = \|r(u,t) - r_0(u)\| + \|z(u,t) - z_0(u)\|, \tag{S55}$$

where $\|f\| = \left(\int_0^1 f(u)^2\, du\right)^{1/2}$ is the L^2 norm of the function f. The stationary state is classified as stable when $\mathrm{dis}(t)$ decays with time, so that the perturbed surface relaxes back to the stationary shape, and unstable when $\mathrm{dis}(t)$ grows and the surface departs from it. Each classification run is integrated for a total duration of $40\,\tau_\eta$, which is long enough for the two behaviours to be distinguished unambiguously. Supplementary Fig. S5 shows $\mathrm{dis}(t)$ for a representative stable and a representative unstable case. The supercritical or subcritical character is determined from the direction and stability of the bifurcating asymmetric branch. The square-root scaling of the ring displacement near the bifurcation is shown in Supplementary Fig. S3.

3.4 Division observables and outcome classification

The furrow position u_{furrow} is defined as the location where the meridional curvature C_u^u is most negative. Its displacement from the equator is

$$\Delta u = u_{\mathrm{furrow}} - 0.5. \tag{S56}$$

Once a narrow neck has formed, the volumes on the two sides of the furrow define the larger and smaller daughter volumes, V_b and V_s, and the division-asymmetry index is

$$\chi = \frac{V_b - V_s}{V_b + V_s}. \tag{S57}$$

When a division proceeds, the furrow radius shrinks toward zero. The computation is stopped once the furrow radius $r_{\mathrm{furrow}} = \min_u r(u,t)$ falls below a numerical cutoff of $0.001\,R_0$, at which point the two sides of the neck are counted as separate daughter cells. Dynamic trajectories that constrict about the equator have $\chi \simeq 0$ and are classified as symmetric division. Trajectories in which the furrow leaves the equator and produces unequal daughter volumes are classified as asymmetric division. Trajectories that instead relax to a weakly invaginated stationary state, without the furrow developing a narrow neck, are classified as failed division; these points are assigned $\chi = 1$ only for visualization in the phase plots and do not represent a completed partition.

3.5 Random perturbation of the initial state

To investigate how sensitively the division outcome depends on the initial condition, we apply a small random perturbation of the active stress at the first time step. Specifically, we replace the active couplings entering the constitutive law of Eq. (S29) by

$$\tilde{\xi}_s \to \tilde{\xi}_s + \sum_{n=1}^{10} a_n \cos(n\pi u), \qquad \tilde{\xi}_b \to \tilde{\xi}_b + \sum_{n=1}^{10} b_n \cos(n\pi u), \tag{S58}$$

where the coefficients are drawn independently for each mode, a_n from a uniform distribution on $[-0.001\,\tilde{\xi}_s,\, 0.001\,\tilde{\xi}_s]$ and b_n from a uniform distribution on $[-0.001\,\tilde{\xi}_b,\, 0.001\,\tilde{\xi}_b]$. The modes $\cos(n\pi u)$ with odd n break the mirror symmetry about the equator. From the second time step onward the perturbation is removed and the couplings revert to their unperturbed values $\tilde{\xi}_s$ and $\tilde{\xi}_b$, so that the subsequent evolution is governed by the unmodified equations and the perturbation acts purely on the initial condition. Each data point in Figs. 2A,G and 3B–E of the main text is obtained from ten independent realizations of this perturbation, and the error bars report the resulting standard deviation.

Supplementary Note 4: Experimental data analysis

4.1 Embryonic morphological datasets

We analyze two published cell-resolved four-dimensional morphological datasets of *C. elegans* embryogenesis: the *CMap* dataset, comprising eight mechanically uncompressed embryos, and the *CShaper* dataset, comprising seventeen mechanically compressed embryos [29,30]. Cell membranes are fluorescently labelled for three-dimensional segmentation and cell nuclei are labelled for lineage tracing. The stereotyped lineage nomenclature provides a common cell identity across embryos and permits the same division event to be compared between samples and mechanical conditions.

4.2 Cell volumes and division asymmetry

Volumes and division asymmetries are computed separately for each embryo. Within a given embryo, the segmented volume of each cell is averaged over all time points in that cell's lifespan. For each division event, the two averaged daughter volumes then give the experimental division-asymmetry index, using the same definition as in the simulations,

$$\chi = \frac{V_b - V_s}{V_b + V_s}. \tag{S59}$$

Every embryo therefore contributes one value of χ per division event, and the statistical unit in the analyses below is a single lineage-resolved division event in a single embryo rather than an individual image frame. The distributions shown in Fig. 5B,D of the main text are taken over these per-embryo values.

In the box plots of Fig. 5B,D of the main text, the box spans the first and third quartiles Q_1 and Q_3, the central line marks the median, and the whiskers extend to the most extreme values lying within $[Q_1 - 3\,\mathrm{IQR},\, Q_3 + 3\,\mathrm{IQR}]$, where $\mathrm{IQR} = Q_3 - Q_1$ is the interquartile range. Values outside this range are plotted individually as outliers.

For the cell-size analysis in Fig. 5B of the main text, somatic cell division events from the uncompressed dataset are grouped into four mother-cell-volume intervals: 10^1–10^2, 10^2–10^3, 10^3–10^4, and 10^4–$10^5\,\mu\mathrm{m}^3$. Adjacent volume groups are compared using a one-sided Wilcoxon rank-sum test. For the P-lineage analysis in Fig. 5D, the division-asymmetry distributions of successive germline cell division events are compared between adjacent events using the same test. The annotations in Fig. 5B,D use n.s. for $p > 0.1$, one asterisk for $p < 0.1$, two asterisks for $p < 0.05$, and three asterisks for $p < 0.001$.

4.3 Compression comparison

To quantify the confinement effect, division events are matched between the uncompressed and compressed datasets by their lineage identity. Each point in Fig. 6B of the main text therefore represents one unique division with asymmetry χ_U in the uncompressed dataset and χ_C in the compressed dataset. Linear regression of the matched values gives the reported slope of 1.151 and $R^2 = 0.917$; the identity line provides the reference for no compression-induced change.

4.4 Cortex-contour comparison and lineage simulation

For the P0 comparison, cell boundaries are obtained from automatic segmentation of the time-lapse images [26]. Experimental and simulated contours are aligned in the same axial cross-section and compared at six matched stages spanning furrow initiation to near-complete division. Let A be the set of pixels enclosed by the experimentally segmented contour and B the set of pixels enclosed by the simulated contour. The similarity index is defined as the fraction of the experimental region that is recovered by the simulation,

$$\text{similarity} = \frac{|A \cap B|}{|A|}, \tag{S60}$$

where $|\cdot|$ denotes the number of pixels in a set. The similarity index shown in Fig. 4A remains above 90% at all displayed stages.

The lineage calculation begins from a single calibrated P0 radius $\tilde{R}_0 = 5.4$ and uses the shared parameter set of Supplementary Table S3 at fixed confinement $\epsilon = 0.87$. Somatic blastomeres divide without the localized polarity profile, whereas the successive P-lineage blastomeres use the localized modulation of $\kappa(u)$. The two daughter volumes computed at each completed division become the mother-cell volumes for the next generation. Lineage termination is set by the cell-size-dependent phase boundary obtained from the bifurcation analysis. At the fixed activity and confinement used here, the critical size $\tilde{R}_{0,c}$ is defined by $\tilde{\xi}_s = \tilde{\xi}_s^*(\tilde{R}_{0,c}, \epsilon)$, where the fixed-activity trajectory crosses the pitchfork boundary separating the asymmetric-division and failed-division regimes. For $\tilde{R}_0 < \tilde{R}_{0,c}$ the mirror-symmetric branch is stable, so the cortex relaxes to a weakly invaginated stationary state without completing division and the corresponding branch is terminated. The boundary relevant to the somatic divisions is the one mapped in Fig. 2A,B of the main text, whereas the polarity-regulated germline divisions terminate at the failure boundary of Fig. 3D, which the localized κ-modulation shifts slightly.

Supplementary Tables

Variation	Implied ODE
$\partial_t r$	$\alpha' = \cdots$
$\partial_t z$	$\beta' = \cdots$
$\partial_t \psi$	$\psi'' = \cdots$
$\partial_t h$	$\zeta' = \cdots$
$\partial_t \alpha$	$r' = \cdots$
$\partial_t \beta$	$z' = \cdots$
$\partial_t \zeta$	$h' = 0$
v^u	$(v^u)'' = \cdots$
v^ϕ	$(v^\phi)'' = \cdots$

Table S1. Structure of the ODE system with differential equations and their corresponding variations.

Variation	Boundary conditions
$\partial_t r$	$r(0) = 0,\ r(1) = 0$
$\partial_t z$	$\beta(0) = 0,\ \beta(1) = 0$
$\partial_t \psi$	$\psi(0) = 0,\ \psi(1) = \pi$
$\partial_t h$	$\zeta(0) = 0,\ \zeta(1) = 0$
v^u	$v^u(0) = 0,\ v^u(1) = 0$
v^ϕ	$v^\phi(0) = 0,\ v^\phi(1) = 0$

Table S2. Boundary conditions arise from boundary terms of the variation Eqs. (S47)-(S51).

Parameter	Biological/Computational Meaning	Value	Unit
κ	Bending rigidity	1	κ_0
η_b	Bulk viscosity	1	η_b
η_s	Shear viscosity	1	η_b
L_h	Hydrodynamic length	1	L_h
τ_η	Time scale	$\eta_b L_h^2/\kappa_0$	τ_η
R_0	Radius of the P0 zygote	5.4	L_h
$\xi_s \Delta\mu$	Symmetric active coupling	25	κ_0/L_h
$\xi_b \Delta\mu$	Bending active coupling	-2.5	κ_0/L_h
Γ	Friction coefficient	1	η_b/L_h^2
ω	Regulation profile width	0.0577	1
Δ_κ	Regulation profile peak	0.1	1
u_0	Regulation position	0.465	1

Table S3. Parameters used in the model. This shared parameter set is used for the lineage-tree simulation of Fig. 4B of the main text, in which R_0 is the radius of the P0 zygote and the cell size decreases from it at each subsequent division.

Supplementary Figures

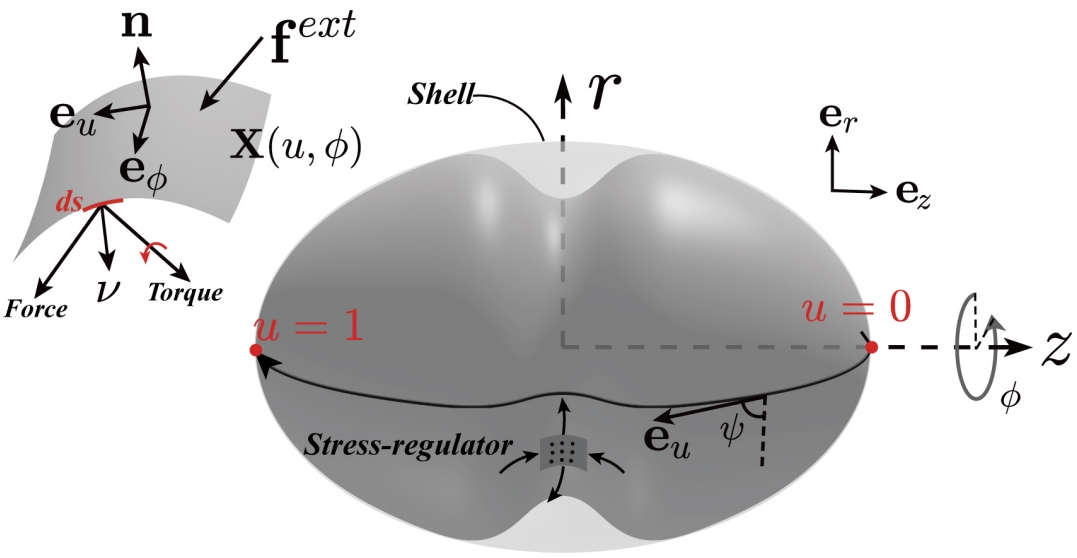


Figure S1. Parameterization of axisymmetric surfaces $\mathbf{X}(u, \phi, \mathbf{t})$. The force and torque are described by the tensors t_{ij} and m_{ij} acting on the line element ds. The geometric shell (semi-transparent gray ellipsoidal shell) is expressed as a potential well outside the enclosed active surface (dark gray opaque solid).

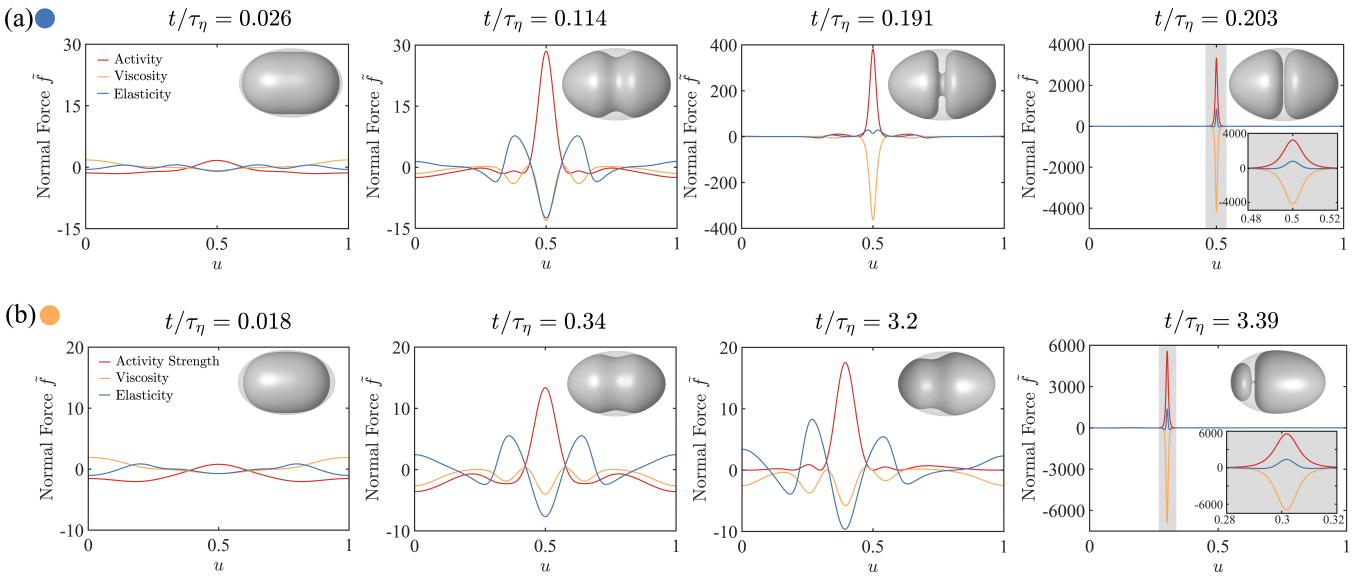


Figure S2. Normal force balance during symmetric and asymmetric division. (a) Symmetric division (blue, $\chi \approx 0$): the dimensionless normal force $\tilde{f}$ decomposed into active (red), viscous (orange), and elastic (blue) contributions, shown at four successive time points spanning the division process (insets: cortex shapes). The furrow forms symmetrically at $u = 0.5$; the active force progressively concentrates at the equatorial region as constriction proceeds. **(b)** Asymmetric division (orange): same force decomposition at four time points. The furrow displaces off the equatorial position; the active and viscous contributions develop an asymmetric spatial profile, and the final panel shows the near-pinched asymmetric furrow (inset, zoomed).

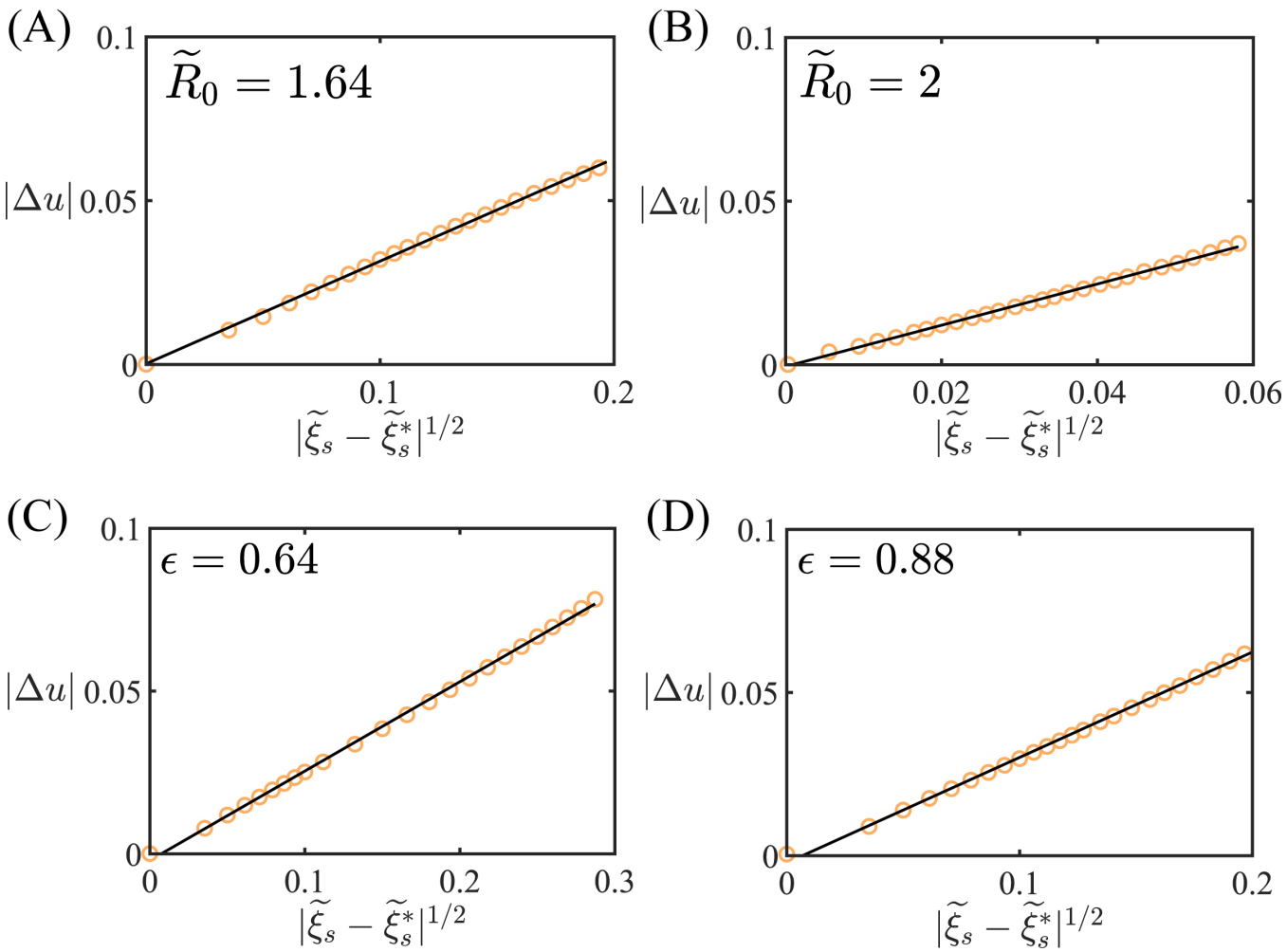


Figure S3. Square-root scaling of the symmetry-breaking bifurcation. Contractile-ring displacement $|\Delta u|$ plotted against $|\tilde{\xi}_s - \tilde{\xi}_s^*|^{1/2}$ for two cell radii (**A**, **B**: $\tilde{R}_0 = 1.64$, 2.00; $\epsilon = 0.87$ fixed) and two confinement levels (**C**, **D**: $\epsilon = 0.64$, 0.88; $\tilde{R}_0 = 2.22$ fixed). Orange circles: numerical data; black lines: linear fits. The linear relationship $|\Delta u| \propto |\tilde{\xi}_s - \tilde{\xi}_s^*|^{1/2}$ confirms that the transition is a pitchfork bifurcation in all cases shown; whether it is supercritical or subcritical is established separately from the branch stability in Fig. 2 of the main text.

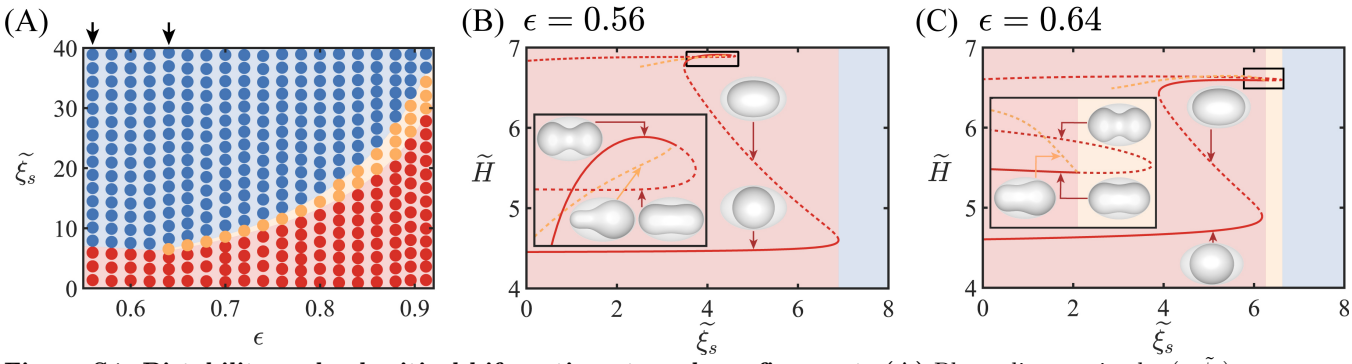


Figure S4. Bistability and subcritical bifurcation at weak confinement. (A) Phase diagram in the $(\epsilon, \tilde{\xi}_s)$ parameter plane, with the same regime colors as Fig. 2 of the main text (blue: symmetric division; orange: asymmetric division; red: failed division). Arrows indicate the two confinement values examined in panels **B** and **C**. **(B,C)** Bifurcation landscapes $\tilde{H}$ vs. $\tilde{\xi}_s$ at $\epsilon = 0.56$ (**B**) and $\epsilon = 0.64$ (**C**). Solid lines: stable branches; dashed lines: unstable branches. In both cases the symmetric branch is S-shaped, with two folding points, one at small $\tilde{H}$ and one at large $\tilde{H}$, whose ordering along $\tilde{\xi}_s$ sets the outcome as $\tilde{\xi}_s$ increases. At $\epsilon = 0.64$ (**C**) the large-$\tilde{H}$ fold lies at the higher $\tilde{\xi}_s$, so the cortex leaves the symmetric branch through a symmetry-breaking bifurcation and passes through an asymmetric-division window before symmetric constriction. At $\epsilon = 0.56$ (**B**) the small-$\tilde{H}$ fold lies at the higher $\tilde{\xi}_s$, so the cortex remains symmetric until that fold and then passes directly to symmetric constriction, with no asymmetric-division window. Arrows indicate the transitions between branches, and insets show representative cortex shapes at selected points.

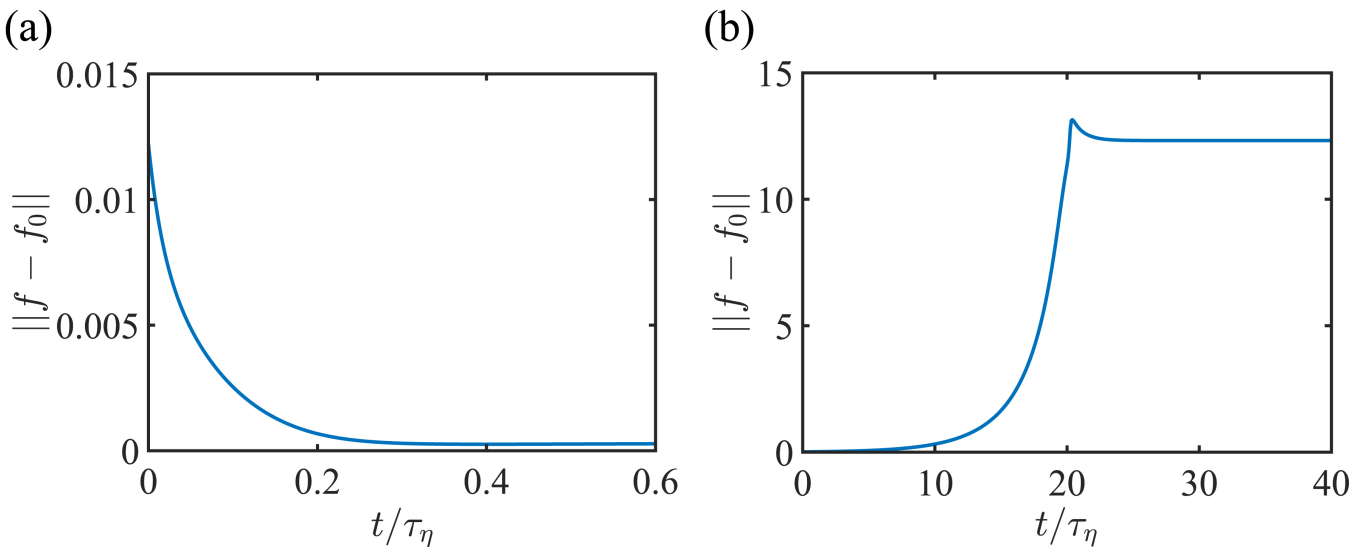


Figure S5. Dynamical classification of the stability of a stationary state. Evolution of the distance $\|f - f_0\|$ between the shape $f = (r, z)$ obtained from the time-dependent simulation and the stationary shape $f_0 = (r_0, z_0)$ used as the initial condition, as defined in Eq. (S55). The simulation is initialized from the stationary state with the small random perturbation of Sec. 3.5. **(a)** Stable case: the distance decays back to zero, so the perturbed surface relaxes to the same stationary shape. Only the initial part of the time window is shown, so that the decay is resolved. **(b)** Unstable case: the distance grows and the surface departs from the stationary state, settling onto a different branch. All stability simulations are run for a total duration of $40\,\tau_\eta$.

Supplementary Movie Legends

Supplementary Movie 1 | Symmetric division at large cell size. Dynamic simulation of a large cell dividing symmetrically. Starting from the ellipsoidal rest shape imposed by the confining shell, activation of the curvature-dependent active stress nucleates a constriction furrow at the equatorial plane that deepens symmetrically, partitioning the cell into two daughters of equal volume. The dark gray surface is the active cortex and the semi-transparent gray ellipsoid is the confining shell; time is given in units of the viscous relaxation time τ_η. This movie corresponds to the symmetric division of Fig. 1C of the main text.

Supplementary Movie 2 | Asymmetric division via spontaneous symmetry breaking. Dynamic simulation of a cell in the symmetry-broken regime. The furrow initially forms near the equator but, as it deepens, spontaneously slips off the equatorial plane and migrates toward one pole, yielding two daughters of unequal volume. Rendering and time units as in Supplementary Movie 1. This movie corresponds to the asymmetric division of Fig. 1D of the main text.

Supplementary Movie 3 | Failed division at reduced cell size. Dynamic simulation of a small cell. The cortex develops only a shallow, weakly invaginated furrow at the equatorial plane that fails to constrict to completion, so that cytokinesis does not proceed. Rendering and time units as in Supplementary Movie 1. This movie corresponds to the failed-division regime of Fig. 2 of the main text.

Supplementary Movie 4 | Reproduction of the P0 zygote division. Dynamic simulation of the first (P0) cleavage of the *C. elegans* embryo using the polarity-regulated model with a localized modulation of cortical bending rigidity. The furrow is biased slightly off the equator, reproducing the mildly asymmetric division that yields the larger AB and smaller P1 blastomeres. Rendering and time units as in Supplementary Movie 1. This movie corresponds to the P0 division of Fig. 4A of the main text.